RESEARCH ARTICLE

Scleraxis-lineage cell depletion improves tendon healing and disrupts adult tendon homeostasis

Katherine T Best[1], Antonion Korcari[1,2], Keshia E Mora[1,2], Anne EC Nichols[1], Samantha N Muscat[1], Emma Knapp[1], Mark R Buckley[1,2], Alayna E Loiselle[1,2]*

[1]Center for Musculoskeletal Research, University of Rochester Medical Center, Rochester, United States; [2]Department of Biomedical Engineering, University of Rochester, New York, United States

Abstract Despite the requirement for *Scleraxis*-lineage (Scx^{Lin}) cells during tendon development, the function of Scx^{Lin} cells during adult tendon repair, post-natal growth, and adult homeostasis have not been defined. Therefore, we inducibly depleted Scx^{Lin} cells ($ScxLin^{DTR}$) prior to tendon injury and repair surgery and hypothesized that $ScxLin^{DTR}$ mice would exhibit functionally deficient healing compared to wild-type littermates. Surprisingly, depletion of Scx^{Lin} cells resulted in increased biomechanical properties without impairments in gliding function at 28 days post-repair, indicative of regeneration. RNA sequencing of day 28 post-repair tendons highlighted differences in matrix-related genes, cell motility, cytoskeletal organization, and metabolism. We also utilized $ScxLin^{DTR}$ mice to define the effects on post-natal tendon growth and adult tendon homeostasis and discovered that adult Scx^{Lin} cell depletion resulted in altered tendon collagen fibril diameter, density, and dispersion. Collectively, these findings enhance our fundamental understanding of tendon cell localization, function, and fate during healing, growth, and homeostasis.

***For correspondence:** alayna_loiselle@urmc.rochester.edu

Competing interests: The authors declare that no competing interests exist.

Funding: See page 30

Received: 17 August 2020
Accepted: 21 January 2021
Published: 22 January 2021

Reviewing editor: Mone Zaidi, Icahn School of Medicine at Mount Sinai, United States

© Copyright Best et al. This article is distributed under the terms of the Creative Commons Attribution License, which permits unrestricted use and redistribution provided that the original author and source are credited.

Introduction

Despite the significant efforts toward improving tendon healing and regeneration, the specific cellular contributions during tendon healing have not been extensively characterized (***Nichols et al., 2019***). While many studies have examined the potential of using various stem cell populations to promote healing, originating from both tendon intrinsic (***Walia and Huang, 2019***) and extrinsic sources (***Costa-Almeida et al., 2019***), little focus has been directed toward defining the functions and therapeutic potential of tendon cells during tendon healing following an acute injury. Tendon cells are increasingly recognized as a heterogenous population of cells where many, but not all, express the gene *Scleraxis* (*Scx*) (***Best and Loiselle, 2019***; ***Kendal et al., 2020***; ***De Micheli et al., 2020***). Understanding the localization and function of tendon cell subpopulations during healing is likely to be instrumental in better defining the mechanisms that promote scar-mediated healing, which results in poor patient outcomes, and could therefore be used to develop pro-regenerative approaches to improve healing.

Scx, a basic helix-loop-helix transcription factor, is currently the most well-characterized marker that the field possesses to study tendon (***Schweitzer et al., 2001***). *Scx* has been utilized to examine tendon biology and development (***Murchison et al., 2007***; ***Pryce et al., 2009***; ***Huang et al., 2019***), healing and regeneration (***Sakabe et al., 2018***; ***Howell et al., 2017***; ***Best and Loiselle, 2019***; ***Dyment et al., 2014***), differentiation (***Bavin et al., 2017***; ***Chen et al., 2012***; ***Alberton et al., 2012***; ***Nichols et al., 2018a***), and mechano-transduction (***Maeda et al., 2011***; ***Nichols et al., 2018b***). Functionally, *Scx* expression can drive matrix production and remodeling (***Sakabe et al., 2018***; ***Leéjard et al., 2007***; ***Levay et al., 2008***), epithelial-to-mesenchymal transition (***Al-Hattab et al.,***

2018), development of force-transmitting tendons (Murchison et al., 2007), tendon growth (Gumucio et al., 2020), and effect focal adhesion morphology (Nichols et al., 2018b). Despite the effort to understand the functions of *Scx* as a transcription factor, the function and requirement of *Scx*-lineage (Scx^{Lin}) cells in tendon repair, post-natal growth, and homeostasis has not been defined.

Previous studies examining the localization and role of tendon cells during healing are limited. *Scx*-GFP mice (Pryce et al., 2007) have been used to visualize tendon cells in many studies; however, previous work has suggested that extrinsic, paratenon-derived *Scx*-GFP^- cells can turn on *Scx* expression and become *Scx*-GFP^+ by 14 days in a Patellar tendon injury model (Dyment et al., 2014). This makes interpretation using *Scx*-GFP mice complicated during in vivo studies as it becomes difficult to determine if a *Scx*-GFP^+ cell is tendon-derived or simply activating *Scx* expression post-injury. Other studies have utilized the inducible Scx-Cre^{ERT2} mouse model to label Scx^+ cells prior to injury to allow tracking of these cells post-injury (Scx^{Ai9}). Howell et al. determined that while *Scx*-GFP cells and Scx^{Ai9} tendon cells localized to the regenerated tendon in neonatal mice, these cells were not recruited to the scar tissue/bridging tissue during adult healing in Achilles tendon (Howell et al., 2017). In contrast, we have previously demonstrated that Scx^{Ai9} tendon cells organize into a linear, cellular bridge spanning the scar tissue between the tendon stubs following acute injury and repair of the adult flexor digitorum longus (FDL) tendon (Best and Loiselle, 2019). While these studies suggest that tendon type (ex. flexor, Achilles, etc.) and injury model-specific (ex. transection with no repair, transection with repair, etc.) differences may modulate the Scx^{Lin} cell contribution to injury, it also highlights the near complete lack of characterization of Scx^{Lin} cell function in the healing process.

In the present study, we hypothesized that Scx^{Lin} tendon cells would be required for successful healing in an adult model of acute flexor tendon repair by driving formation of a collagenous tissue bridge. We utilized a genetic mouse model of Scx^{Lin} cell depletion to directly assess the function of tendon cells during healing and surprisingly discovered that depletion of Scx^{Lin} tendon cells resulted in improved tendon biomechanical properties. We also examined alterations in wound healing-related cell populations, transcriptomics via RNA sequencing, and the effects of Scx^{Lin} cell depletion on tendon post-natal growth and homeostasis.

Results

Successful ablation of *Scleraxis*-lineage tendon cells using diphtheria toxin receptor mouse model

To determine the feasibility of depleting tendon cells using Scx-Cre; Rosa-DTR^{LSL} ($ScxLin^{DTR}$) mice (Figure 1A), diphtheria toxin (DT) was administered into the right hind paw for 5 consecutive days. Ten days after the final DT injection, both the injected and contralateral control hind paws were harvested (Figure 1B). This approach resulted in 57% depletion of tendon cells in uninjured $ScxLin^{DTR}$ FDL tendons relative to WT control littermates ($p<0.0001$) (Figure 1C and D). Tendon cell number was unaffected in the contralateral FDL, indicating that local DT injections did not induce cell death in locations other than the targeted hind paw (Figure 1C and D).

To better understand how this depletion regimen specifically effects Scx^{Lin} cells we used Scx-Cre; Rosa-DTA^{LSL}; Rosa-Ai9 reporter mice ($ScxLin^{Ai9DTR}$) (Figure 1E). Samples were harvested at 24 and 38 days post-depletion (Figure 1F). At 24 days post-depletion, there was a 58.9% reduction in total tendon cells in uninjured $ScxLin^{Ai9DTR}$ FDL tendons relative to WT control littermates ($p<0.0105$) and a 68.48% depletion of Scx^{LinAi9} cells in $ScxLin^{Ai9DTR}$ FDL tendons relative to WT $ScxLin^{Ai9}$ controls ($p<0.0068$) (Figure 1G and H). At 38 days post-depletion, total tendon cells were reduced by 60.42% ($p<0.0091$), and Scx^{LinAi9} cells were reduced by 73.65% relative to $ScxLin^{Ai9}$ WT controls ($p<0.0045$) (Figure 1G and H). No significant differences in total tendon cell depletion efficiency ($p<0.9935$) and Scx^{LinAi9} cell depletion efficiency ($p<0.9359$) were found between D24 and D38 post-depletion timepoints.

To understand how $ScxLin^{DTR}$ affected previously established tendon cell sub-populations (Best and Loiselle, 2019), we evaluated active Scx and S100a4 expression in $ScxLin^{DTR}$ and WT uninjured flexor tendons 10 days following the final DT injection. The number of Scx+ cells was significantly reduced in the $ScxLin^{DTR}$ tendons relative to WT littermates, as expected ($p=0.0448$) (Figure 1—figure supplement 1A &B). Similarly, when Scx+ cells were normalized to total cell

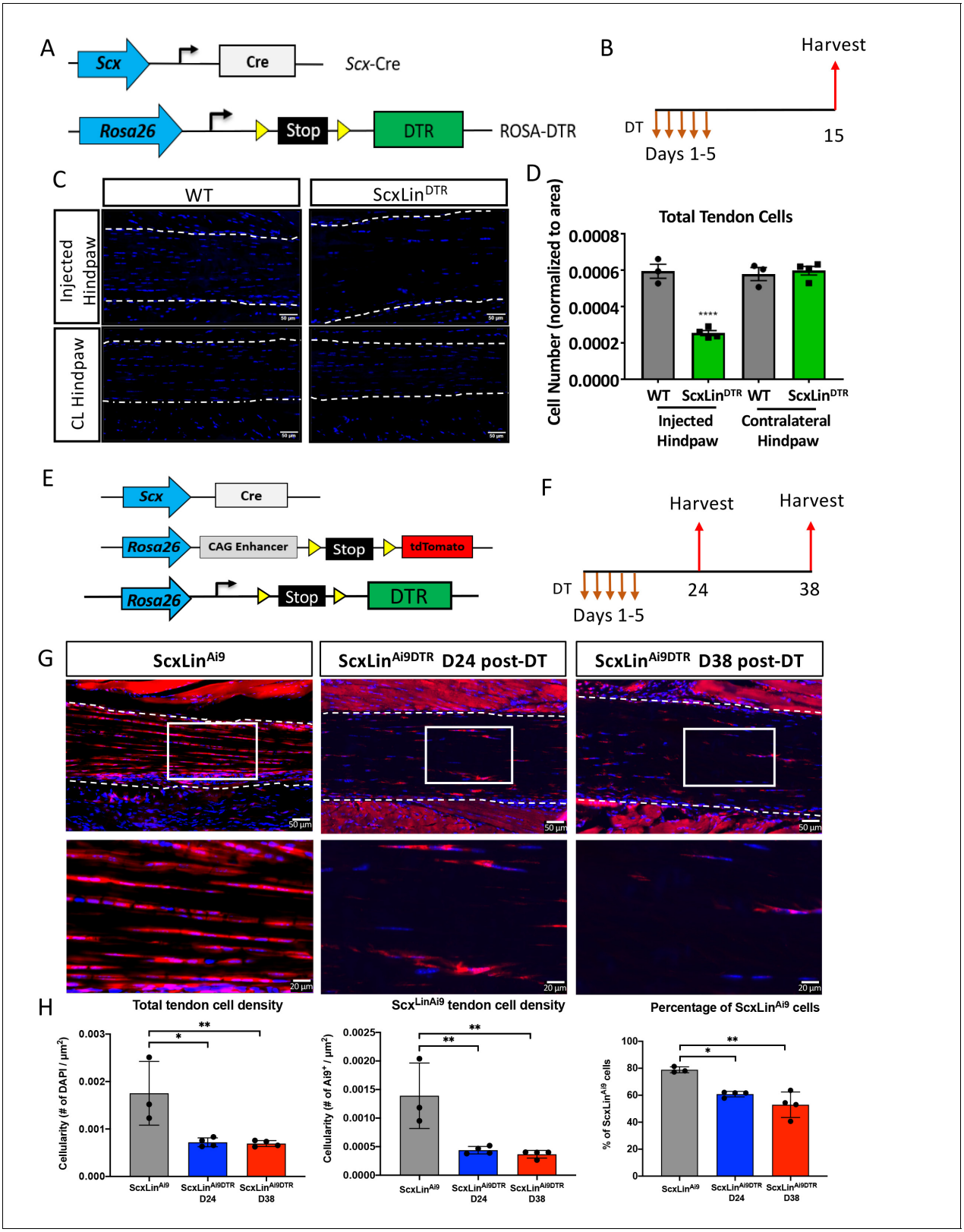

Figure 1. Efficiency of tendon cell and Scx^{Lin} cell depletion. (**A**) To deplete Scx^{Lin} cells, Scx-Cre mice were crossed to the diphtheria toxin receptor mouse (ScxLin^{DTR}). (**B**) Mice received five hind paw injections of DT and were harvested 10 days after the final injection. (**C**) Sections from injected and contralateral (CL) hind paws from WT and ScxLin^{DTR} mice were stained with DAPI, and total DAPI+ cells within the tendon (white outline) were quantified (**D**). (**E**) To determine the depletion efficiency specifically of Scx^{Lin} cells, Scx-Cre; Rosa-DTR^{LSL}; Rosa-Ai9 and Scx-Cre; Rosa-Ai9 reporter mice

Figure 1 continued on next page

Figure 1 continued

were given local, daily DT injections for 5 consecutive days and hind paws were harvested 24 and 38 days after the last injection (**F**) These are the contralateral control tendons from the mice in ***Figure 4*** that underwent tendon injury and repair. (**G**) Hind paws from ScxLin^{Ai9} and ScxLin^{Ai9DTR} were probed for Red Fluorescent Protein (RFP; Ai9) expression and counterstained with the nuclear dye DAPI. (**H**) Total tendon cell density (DAPI^{+}), total ScxLin^{Ai9+} cell density and the percentage of ScxLin^{Ai9} cells (ScxLin^{Ai9+} cells/ DAPI^{+} cells) were quantified in ScxLin^{Ai9} and ScxLin^{Ai9DTR} tendons and demonstrate a significant reduction of ScxLin^{Ai9} cells in ScxLin^{Ai9DTR} relative to ScxLin^{Ai9} WT controls. N = 3–4 per genotype. Two-way ANOVA with Sidak's multiple comparisons test used to assess statistical significance of tendon cell ablation between hind paw (injected with DT or contralateral) and genotype (ScxLin^{Ai9} and ScxLin^{Ai9DTR} at 24 and 38 days). * indicates p<0.05 for the indicated comparison, ** indicates p<0.01 for indicated comparison, **** indicates p<0.0001 relative to all other groups.

The online version of this article includes the following figure supplement(s) for figure 1:

Figure supplement 1. *Scx+* and *S100a4+* tendon cells following Scx^{Lin} depletion.

Figure supplement 2. ScxLin^{DTR} does not cause substantial effects on surrounding tissue.

count, there was a trending reduction of Scx+ cells in ScxLin^{DTR} tendons compared to WT (p=0.1000) (***Figure 1—figure supplement 1C***). ScxLin^{DTR} tendons had a trending decrease in S100a4+ cells relative to WT littermates (p=0.0941) (***Figure 1—figure supplement 1D &E***). Interestingly, when S100a4+ cells were normalized to total cell count, there was no significant or trending difference between groups (p=0.3525), suggesting some remaining tendon cells may begin expressing S100a4 following Scx^{Lin}cell depletion (***Figure 1—figure supplement 1F***). ScxLin^{DTR} tendons exhibited a small number of apoptotic cells peripheral to, but not within, the tendon suggesting that a 10-day DT washout period was sufficient for all tendon-specific DT-induced cell death to occur (***Figure 1—figure supplement 2A***). Both ScxLin^{DTR} and WT littermates exhibited PCNA+ cells within the muscle, but not within then tendon, and ScxLin^{DTR} exhibited a few PCNA+ cells within the tendon that were not present in WT (***Figure 1—figure supplement 2B***). ScxLin^{DTR} tendons exhibited more F4/80+ macrophages peripheral to the tendon, potentially due to macrophage recruitment to the tendon to clean up apoptotic tendon cell debris (***Figure 1—figure supplement 2C***).

Ablation of Scleraxis-lineage cells results in significantly increased biomechanical properties by day 28 post repair while not affecting gliding function

To define the functional effects of Scx^{Lin} cell depletion on tendon healing, mice received five local DT injections to deplete Scx^{Lin} cells followed by FDL repair 10 days following the final injection (***Figure 2A***). A trending improvement in MTP Range of Motion (ROM) in ScxLin^{DTR} repairs was observed at day 14, relative to WT littermates (WT vs ScxLin^{DTR}, p=0.0711), but this trend was absent by day 28 post-repair (***Figure 2B***). ScxLin^{DTR} healing tendons did not significantly differ in gliding resistance at either day 14 or 28 post-repair (***Figure 2C***). While biomechanical properties were not altered between groups at day 14, both stiffness and maximum load at failure were significantly increased in ScxLin^{DTR} healing tendons relative to wildtype littermates at day 28 post-repair (Stiffness: WT: 6.48 ± 0.75, ScxLin^{DTR}: 11.22 ± 1.83, p=0.0237; Maximum load at failure: WT: 1.54 ± 0.17, ScxLin^{DTR}: 2.44 ± 0.24, p=0.0061) (***Figure 2D and E***). Between days 14 and 28, WT tendon stiffness increased by 39.06% while ScxLin^{DTR} stiffness increased by 109.33%, and WT tendon maximum load at failure increased by 52.48% while ScxLin^{DTR} maximum load at failure increased by 162.37%, indicating that ScxLin^{DTR} repairs heal at an accelerated rate relative to wild-type littermates.

Scleraxis-lineage cells are not required for the formation of a bridging collagen matrix during tendon healing

We have previously demonstrated that a cellular bridge corresponds to a region of bridging collagen matrix in the scar tissue (***Best and Loiselle, 2019***). While there were no apparent differences in tissue morphology between groups at days 14 or 28 post-repair (***Figure 3B***), we wanted to determine if tendon cell depletion prevented formation of the collagen bridge. Masson's trichrome staining revealed presence of bridging collagen through the scar in both groups at days 14 and 28, indicating that depletion of Scx^{Lin} tendon cells does not prevent formation of the bridging collagen matrix (***Figure 3C***).

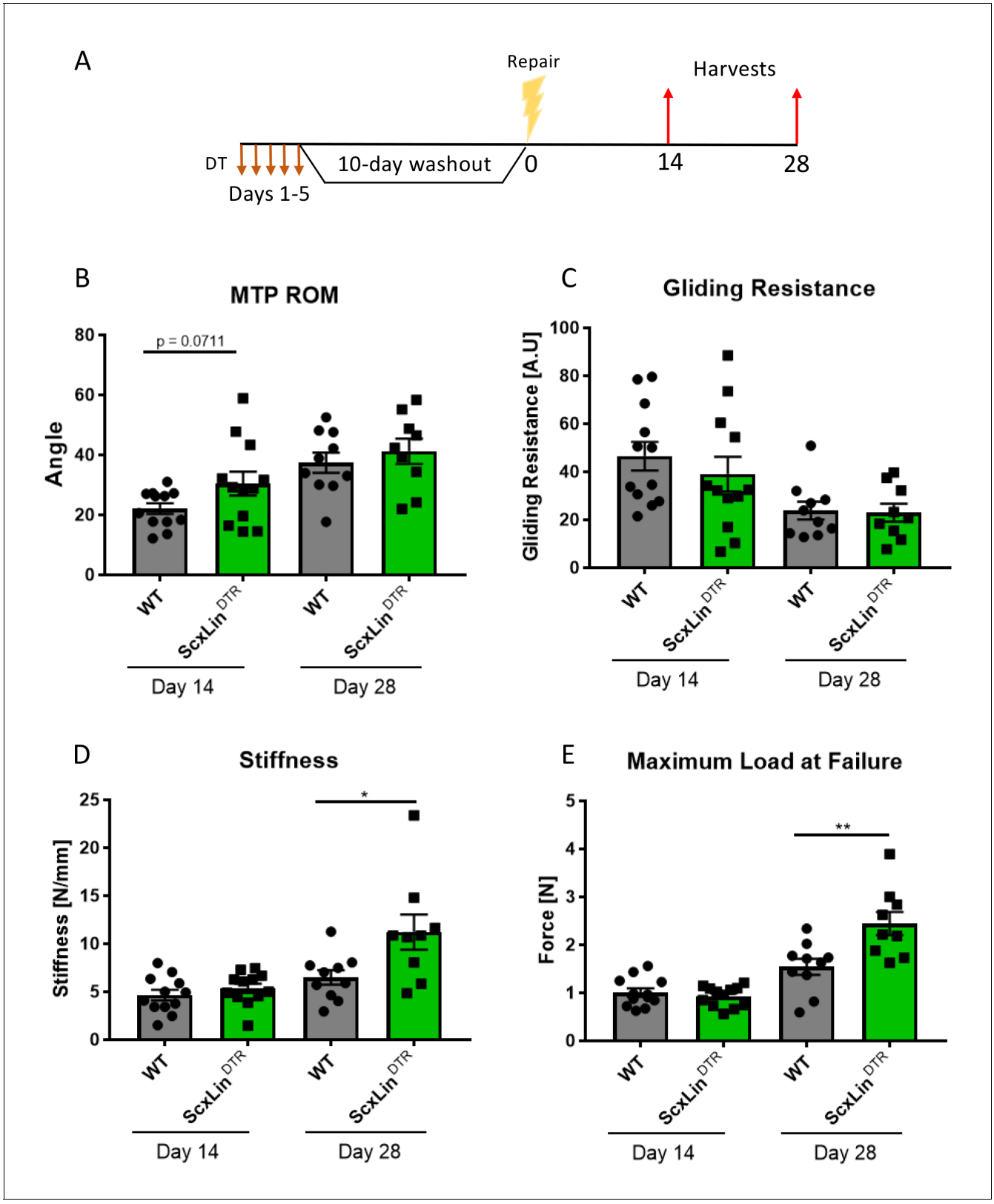

Figure 2. ScxLin^{DTR} tendons heal with significantly increased biomechanical properties. Mice received five hind paw injections of DT on consecutive days, underwent flexor tendon repair surgery 10 days after the final DT injection, and were harvested at 14- and 28 days post-repair (**A**). Measurement of metatarsophalangeal (MTP) joint flexion angle (**B**), gliding resistance (**C**), stiffness (**D**), and maximum load at failure (**E**) of WT and ScxLin^{DTR} repaired

Figure 2 continued on next page

Figure 2 continued

tendons. N = 9–12 per genotype per timepoint. Students t-test used to assess statistical significance between genotypes at a given timepoint. * indicative of p<0.05, ** indicative of p<0.01.

Scx^{Lin} cell depletion results in a significant lower *Scx*$^{lin+}$ cells during tendon healing

To better understand how depletion of Scx^{Lin} cells prior to injury and repair affected Scx^{Lin} cell density during healing, we traced Scx^{LinAi9} cells at D14 and D28 post-injury (***Figure 4A***) No significant differences in Scx^{LinAi9} cells were detected between WT (ScxLin^{Ai9}) and ScxLin^{Ai9DTR} (p=0.3115) at D14 post-surgery (***Figure 4B,C***). In contrast, at D28 post-surgery, a significant decrease in Scx^{LinAi9} cells was observed in ScxLin^{Ai9DTR} repairs (p<0.0034) relative to WT repairs (***Figure 4B,D***). Collectively, these data suggest that depletion of ScxLin^{Ai9} cells prior to injury does not alter the overall ScxLin^{Ai9} content at D14, possibly due to additional labeling of cells that express *Scx* following injury. In contrast, by D28 the effects of depleting ScxLin^{Ai9} cells prior to tendon injury is manifested in changes in both ScxLin^{Ai9} content (***Figure 4B,D,E***) and phenotypic differences (***Figure 2***).

Scx^{Lin} depletion enhances myofibroblast content during tendon healing

We have previously demonstrated that elevated F4/80+ macrophages and αSMA+ myofibroblasts are associated with increased tendon maximum load at failure (***Best et al., 2019***). No significant differences in F4/80+ macrophages were detected between genotypes at either day 14 or 28 post-repair (***Figure 5B***). While αSMA+ myofibroblasts were not significantly altered at day 14 (D14: WT vs DTR, p=0.3790), ScxLin^{DTR} healing tendons had significantly increased levels of αSMA+ myofibroblasts relative to wildtype littermates at D28 (p=0.0188) (***Figure 5C***). We have previously demonstrated that S100a4 is an important molecule that can influence tendon biomechanical properties and gliding function during healing (***Ackerman et al., 2019***). No differences in S100a4+ cells were observed in ScxLin^{DTR}, relative to WT at either day 14 or 28 post-repair (***Figure 5D***). Thus, αSMA+ myofibroblasts are the most likely candidate driving the increased biomechanical properties seen in ScxLin^{DTR} healing tendon, of the cell populations investigated, consistent with their roles in with matrix deposition, organization, and contraction. To demonstrate both the specificity of the αSMA^{+} myofibroblast response to injury and that this tendon injury and repair model does not induce degeneration of the proximal/ distal ends of the tendon due to altered loading, we examined αSMA expression adjacent to the repair site. No αSMA staining was observed in the proximal/distal native tendon away from the repair site at D14 or D28 (***Figure 5—figure supplement 1***).

Identification of differentially expressed genes following Scx^{Lin} depletion

To further investigate the mechanisms driving altered biomechanical properties of healing ScxLin^{DTR} tendons, bulk RNAseq analysis was conducted on days 14 and 28 post-repair samples from ScxLin^{DTR} and WT. A total of three biological replicates per genotype per timepoint were submitted for analysis. At 14 days post-repair, 47 genes were up-regulated, and 313 genes were down-regulated in ScxLin^{DTR} relative to WT (***Figure 6A,B***). At 28 days post-repair, 1237 genes were up-regulated, and 1296 genes were down-regulated in ScxLin^{DTR} relative to WT (***Figure 6C,D***). Based on both the low number of differentially expressed genes (DEGs) and the lack of mechanical phenotype at D14 between WT and ScxLin^{DTR} (***Figure 2***), our primary RNAseq analyses were focused on day 28.

Scx^{Lin} depletion drives differential expression of matrix-related gene expression

The day 28 dataset was analyzed using ingenuity pathway analysis (IPA) software. We hypothesized that a change in the matrix composition could be driving the altered biomechanical properties detected at day 28 post-repair in ScxLin^{DTR} animals, possibly driven by the elevated myofibroblast content. To examine the biological effects of Scx^{Lin} cell depletion at the transcriptional level, downstream effects analysis was performed by utilizing the core analysis in IPA where activation states were assigned for biological processes with p-value<0.05 and z-score $\geq$ 2 (***Table 1***). Included in the

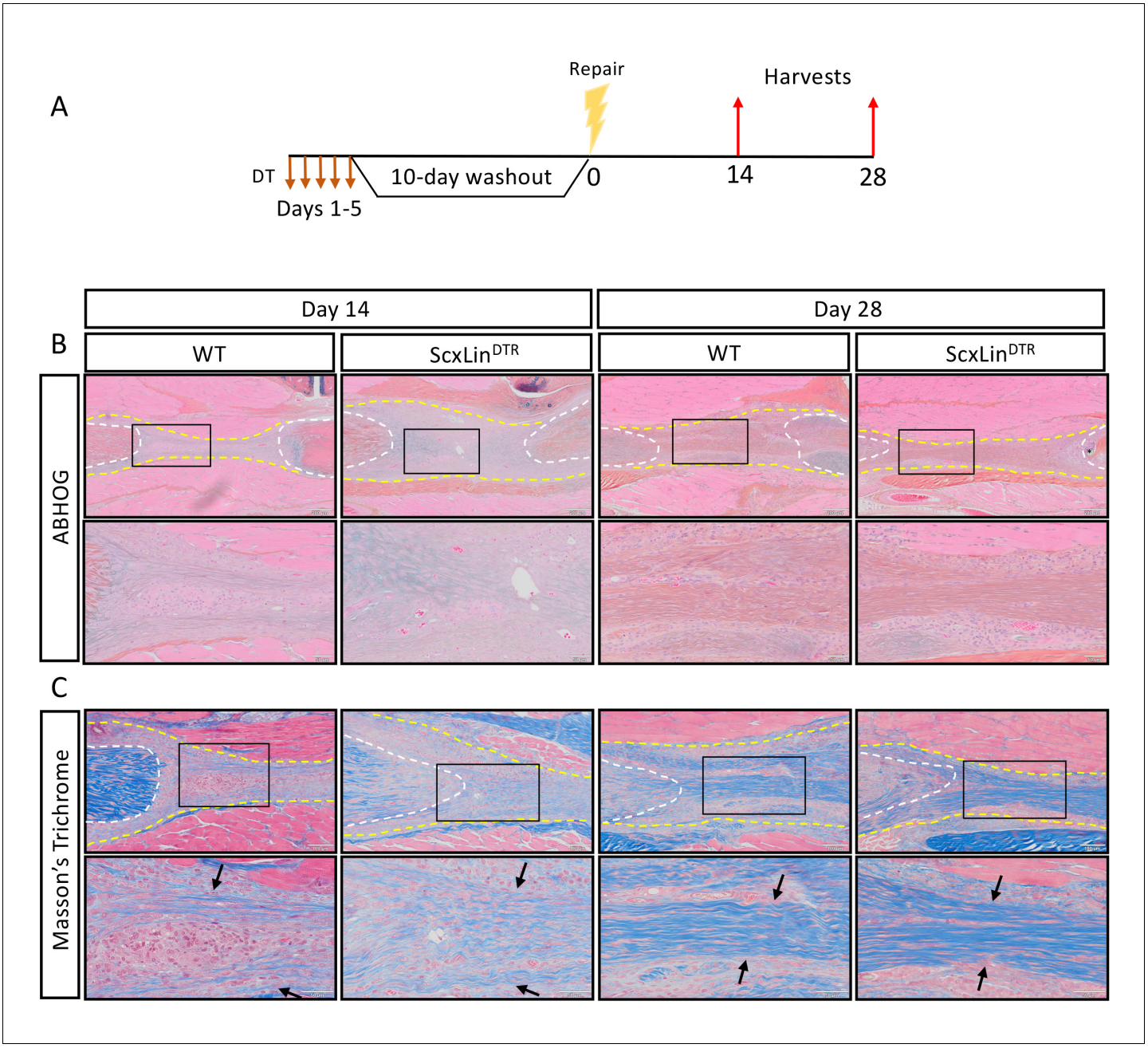

Figure 3. Scx^{Lin} cell depletion does not disrupt formation of a bridging collagen matrix. Mice received five hindpaw injections of DT on consecutive days, underwent flexor tendon repair surgery 10 days after the final DT injection, and were harvested at 14 and 28 days post-repair (**A**). Alcian blue/hematoxylin and Orange G stain utilized to assess overall morphology (**B**). Masson's trichrome stain used to visualize collagen content and organization (**C**). Tendon is outlined by white dotted line and scar tissue by yellow dotted line. Black boxes indicate location of higher magnification images. Boundaries of bridging collagen indicated by black arrows. N = 4 genotype per timepoint. Suture indicated by *.

significantly increased disease and function annotations was 'Fibrosis' (p=3.37E-07, Z = 2.397, ***Table 1***). As we have already demonstrated that depletion of Scx^{Lin} cells is not driving increased fibrotic healing (***Figure 2B,C***), we then examined if the significantly increased 'Fibrotic' annotation was indicative of altered expression of specific matrix-associated genes. Utilizing the comprehensive review of the matrisome by ***Hynes and Naba, 2012***, genes coding for collagens, proteoglycans, basement membrane proteins, and glycoproteins were compiled and examined (***Table 2***). Many matrix-related genes were significantly increased in ScxLin^{DTR} repairs relative to WT littermates at

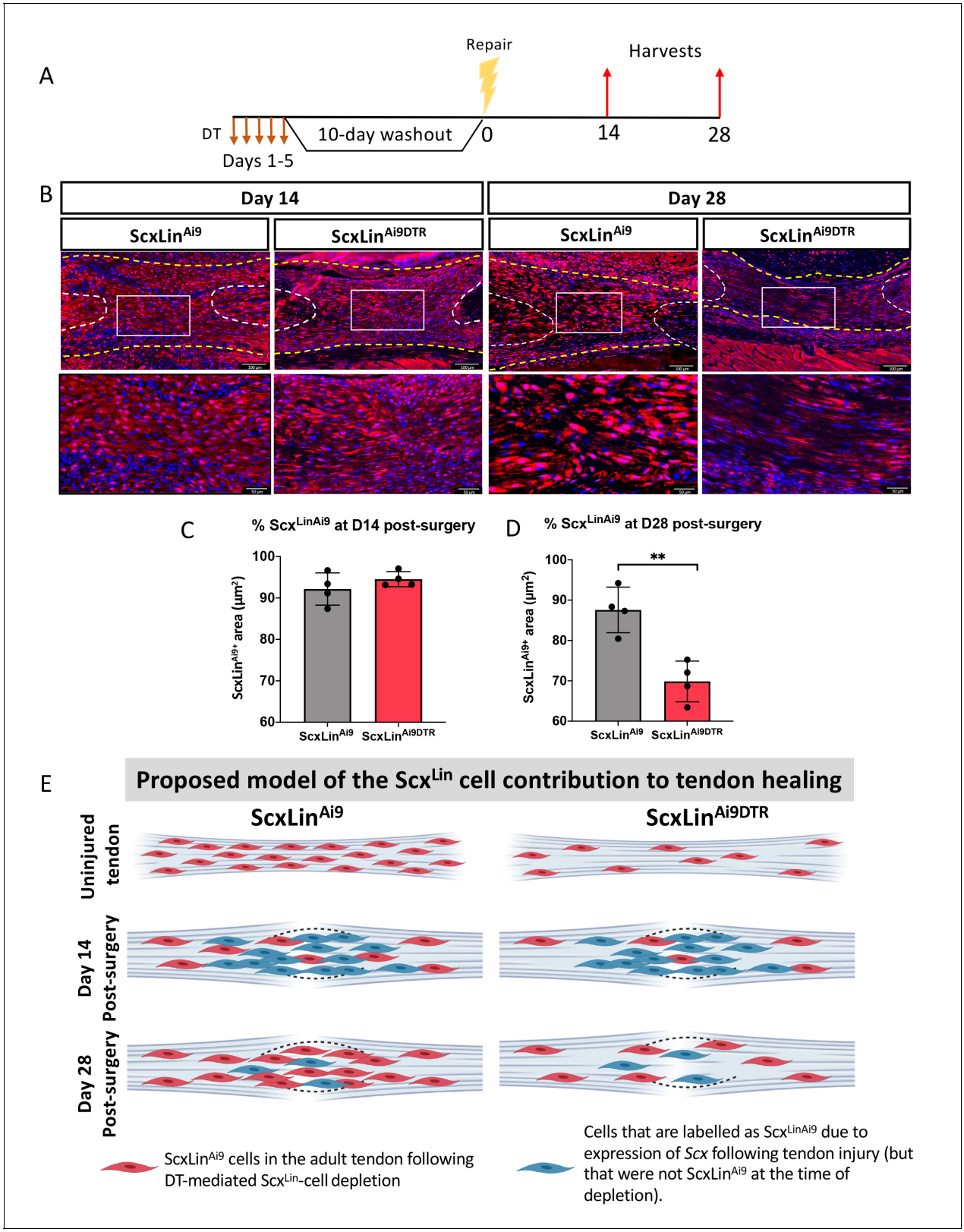

Figure 4. Scx^{Lin} cell depletion results in time-dependent changes in ScxLin^{Ai9} cell presence during tendon healing. (**A**) Mice received hind paw injections of DT on 5 consecutive days, underwent flexor tendon repair surgery 10 days after the final DT injection, and were harvested at 14 and 28 days post-repair. (**B**) Immunofluorescence for RFP (Ai9) in WT ScxLin^{Ai9} and ScxLin^{Ai9DTR} tendon repairs at 14 and 28 days post-repair to define changes in ScxLin^{Ai9} contribution following Scx^{Lin} cell depletion. Quantification of Scx$^{LinAi9+}$ area in ScxLin^{Ai9} WT repairs and ScxLin^{Ai9DTR} repairs at (**C**) D14 and

Figure 4 continued on next page

Figure 4 continued

(**D**) D28 post-surgery. Nuclei were stained with DAPI. N = 4 per genotype. Student's t-test used to assess statistical significance between genotypes at a given timepoint. **indicates p<0.01. (**E**) Proposed model of the time-dependent contributions of ScxLin^{Ai9} cells to the tendon healing process. During adult tendon homeostasis ScxLin^{Ai9} cells are the predominant tenocyte population and ScxLin^{Ai9DTR} results in depletion of ~60% of these cells. Red cells indicate ScxLin^{Ai9} cells that were present in the tendon when depletion was initiated. We hypothesize that no differences in the proportion of ScxLin^{Ai9} cells is observed at D14 (concomitant with a lack of functional phenotypic differences) due to the predominance and functions of other cell populations, including those that express *Scx* in response to injury and are therefore labeled as Scx^{Lin} (blue cells). In contrast, we hypothesize that by D28 the contribution of 'new' Scx^{Lin} cells (blue cells) has waned, and that the ScxLin^{Ai9} cells that were present in the tendon during adult tendon homeostasis (red cells) are now the predominant tenocyte population and exert their functions at this time as suggested by functional differences between WT and ScxLin^{DTR} at this time. This schematic was made using http://www.biorender.com.

day 28 post-repair (ex. *Col1a2, Col3a1, Col8a1, Epyc, Thbs4,* complete list in ***Table 2***), while other matrix components were significantly decreased (ex. *Col6a4, Col9a1, Fras1*, complete list in ***Table 2***). To both validate the RNAseq data and to define the spatial localization of different matrix components, we performed immunofluorescence for Decorin (Dcn), Thbs4 and Mfap5. Both the staining intensity and staining extent of Dcn, Thbs4 and Mfap5 were substantially increased in D28 ScxLin^{DTR} repairs, relative to WT (***Figure 6—figure supplement 1***), consistent with the increases in these matrix components identified by RNAseq (***Table 2***).

Effects on cell motility, cytoskeletal organization, metabolism, and oxidative stress identified in ScxLin^{DTR} repair tendons

Utilizing the downstream effects analysis described above (***Table 1***), we next examined other significantly altered biological functions in ScxLin^{DTR} tendon repairs relative to WT. The inhibited pathways indicated decreased contractility and function of muscle (ex. 'Contractility of skeletal muscle,' p=4.96E-16, Z = −3.595) and decreased oxygen consumption ('Consumption of Oxygen,' p=9.42E-07, Z = −2.237) in ScxLin^{DTR} tendons relative to wildtype controls at day 28 post-repair (***Table 1***). While only 14 disease and function annotations were found to be inhibited, 62 annotations were found to be significantly activated. Interestingly, in addition to 'Fibrosis,' the activated biological pathways indicated increased cell movement and migration (ex. 'Migration of cells,' p=6.44E-17, Z = 4.733), reorganization of the cytoskeletal network (ex. 'Organization of cytoskeleton,' p=2.94E-20, Z = 3.384), metabolism disorders (ex. 'Glucose metabolism disorder,' p=5.46E-10, Z = 3.516), and production of reactive oxygen species (ex. 'Production of reactive oxygen species,' p=6.22E-12, Z = 2.625) (***Table 1***).

Differentially enriched canonical pathways following Scx^{Lin} cell depletion prior to flexor tendon repair

To better understand signaling cascades that could be driving alterations in ScxLin^{DTR} healing, enriched canonical pathways were identified using IPA core analysis. Nineteen canonical pathways were identified, where 13 were positively enriched (activated) and 6 were negatively enriched (inhibited/suppressed) (***Figure 7***, ***Table 3***). Consistent with the metabolism disorders identified from the downstream effects analysis (***Table 2***), canonical pathways related to metabolism were negatively enriched (ex. 'Oxidative Phosphorylation,' -log(p)=7.6, Z = −5.303; additional pathways provided in ***Figure 7*** and ***Table 3***). Additionally, calcium signaling was found to be negatively enriched ('Calcium Signaling,' -log(p)=5.72, Z = −2.335) (***Figure 7*** and ***Table 3***).

Consistent with reorganization of the cytoskeletal network identified from the downstream effects analysis (***Table 2***), numerous canonical pathways related to actin nucleation and polymerization were positively enriched (***Figure 7*** and ***Table 3***). These include 'Rac Signaling' (-log(p)=3.85, Z = 3.674), 'RhoA Signaling' (-log (p) = 3.97, Z = 2.502), and 'Ephrin B Signaling' (-log(p)=3.09, Z = 2.53). Other pathways that are significantly enriched in ScxLin^{DTR} day 28 post-repair tendons include, but are not limited to, 'sphingosine-1-phosphate signaling' (-log(p)=3.94, Z = 2.711) and 'production of nitric oxide and reactive oxygen species in macrophages' (-log(p)=2.01, Z = 2.117) (***Figure 7*** and ***Table 3***).

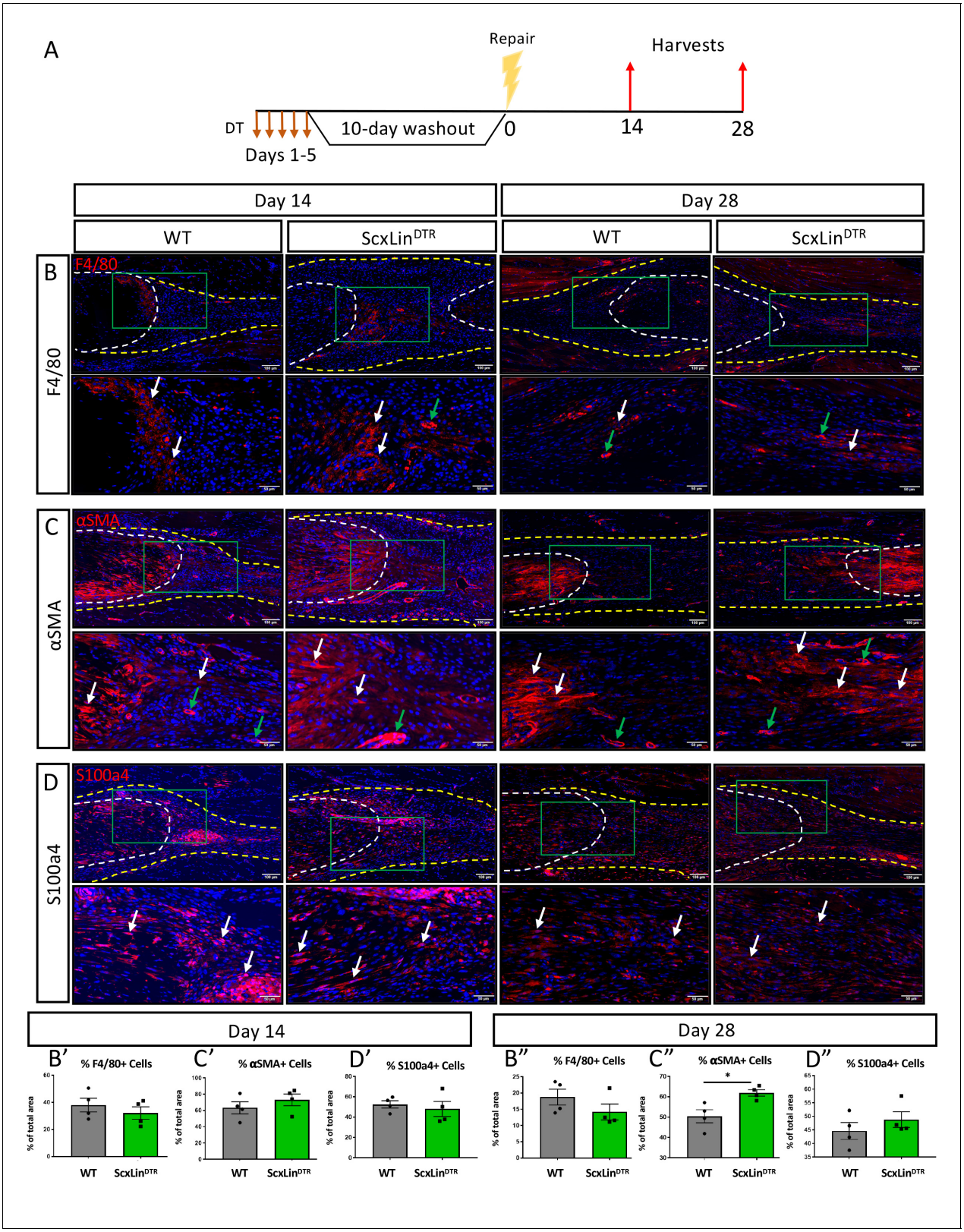

Figure 5. ScxLin^{DTR} repaired tendons heal with increased presence of αSMA+ myofibroblasts. Mice received five hindpaw injections of DT on consecutive days, underwent flexor tendon repair surgery 10 days after the final DT injection, and were harvested at 14 and 28 days post-repair (**A**). Immunofluorescence of WT and ScxLin^{DTR} repair tendons 14 and 28 days post-repair to assess F4/80+ macrophages (**B**), αSMA+ myofibroblasts (**C**), and S100a4+ cells (**D**). Tendon is outlined by white dotted line and scar tissue by yellow dotted line. Green boxes indicate location of higher

Figure 5 continued on next page

Figure 5 continued

magnification images. Examples of positive stain indicated by white arrows, while examples of auto-fluorescent blood cells and α-SMA+ blood vessels indicated by green arrows. Quantification of F4/80 (A' and A''), αSMA (B' and B''), and S100a4 (C' and C'') fluorescence. N = 4 per genotype per timepoint. Student's t-test used to assess statistical significance between genotypes at a given timepoint, except for D28 F4/80 and S100a4 which required a Mann-Whitney test. * indicates $p<0.05$.

The online version of this article includes the following figure supplement(s) for figure 5:

Figure supplement 1. Specific localization of αSMA staining at the tendon repair site.

Identification of possible upstream regulators driving altered ScxLin^{DTR} flexor tendon healing

To identify key molecules that may be driving ScxLin^{DTR} tendon healing at day 28 post-repair, predicted upstream regulators were identified using IPA core analysis. Eight possible activated upstream regulators and four inhibited upstream regulators were identified (***Table 4***). The eight activated regulators included the calcium-binding protein S100a4, peptidase F2, receptors BTNL2 and F2R, transcription factors EBF2 and SOX2, the kinase NTRK2, and growth factor FGF2. The four inhibited regulators included enzyme LDHB and transcription factors FOXO4, MEF2C, and SMYD1.

Ablation of Scx^{Lin} tendon cells does not significantly affect tendon post-natal growth 3 months post-ablation

In addition to roles in tendon healing, *Scx* expression is required for appropriate tendon development and growth processes (***Murchison et al., 2007***; ***Gumucio et al., 2020***). However, the role of Scx+ cells during post-natal growth and adult homeostasis have not been evaluated. Local injection of DT into pre-pubescent mice (3–4 weeks old) resulted in 55% depletion of tendon cells in uninjured ScxLin^{DTR} FDL tendons relative to WT littermates ($p=0.0007$) (***Figure 8A–C***). To assess the requirement for tendon cells in post-natal growth, pre-pubescent mice who were still undergoing periods of rapid growth were injected with DT and harvested at the 3 month timepoint (ScxLin^{DTR,3weeks}) (***Figure 8D***). ScxLin^{DTR,3weeks} tendons did not exhibit an influx of F4/80+ macrophages or tendon cell differentiation into αSMA+ myofibroblasts in either genotype (***Figure 8E***); however, ScxLin^{DTR} mice had a 42.5% decreased tendon cell number relative to WT littermates ($p=0.0454$) demonstrating that the tendon cell environment was not repopulated following depletion (***Figure 8E and F***). There were no significant changes in MTP range of motion, gliding resistance, stiffness, or maximum load at failure between groups (***Figure 8G–J***). Second harmonic generation revealed no significant differences in collagen fibril dispersion between genotypes (***Figure 8K and L***). Taken together, these data suggest that Scx^{Lin} cells are not required for early post-natal tendon growth.

Ablation of Scx^{Lin} tendon cells significantly affected tendon homeostasis 3 months post-depletion

To assess the requirement for Scx^{Lin} tendon cells in maintaining adult tendon homeostasis, 10–12 week-old WT and ScxLin^{DTR} mice were injected with DT to induce cell death and harvested after 3 months (ScxLin^{DTR,10weeks}) (***Figure 9A***). ScxLin^{DTR,10weeks} mice had a 62.3% decrease in tendon cell number relative to WT littermates ($p<0.0001$)(***Figure 9B and C***), demonstrating that tendon cell number had not rebounded in the three months since initial depletion (***Figure 1***). Interestingly, we consistently observed a significant accumulation of unidentified cells on the top and bottom regions of ScxLin^{DTR,10weeks} tendons (***Figure 9B***). Quantification of the cellular density revealed a significant increase on the top ($p<0.0001$) and bottom ($p<0.01$) regions of the ScxLin$^{DTR,10\ weeks}$ compared to WT littermates (***Figure 9D***). ScxLin^{DTR,10weeks} tendons did not exhibit an influx of F4/80+ macrophages or tendon cell differentiation into αSMA+ myofibroblasts in either genotype (***Figure 9E***). Functionally, there were no significant changes in tendon gliding function or biomechanical properties between genotypes after 3 months (***Figure 9F–I***). However, second harmonic generation imaging revealed a significant increase in overall collagen fibril dispersion in ScxLin^{DTR,10weeks} relative to WT littermates (WT: 8.327 degrees ± 0.39, ScxLin^{DTR,10weeks}: 9.815 degrees ± 0.53, $p=0.0393$) (***Figure 9J and K***). Based on the spatial changes in cellularity (***Figure 9D***), we also quantified fibril dispersion in a more spatially specific manner (top, middle and bottom thirds of the tendon) (***Figure 9—figure supplement 1A–D***). Interestingly, the top third of ScxLin^{DTR,10weeks} tendons showed a

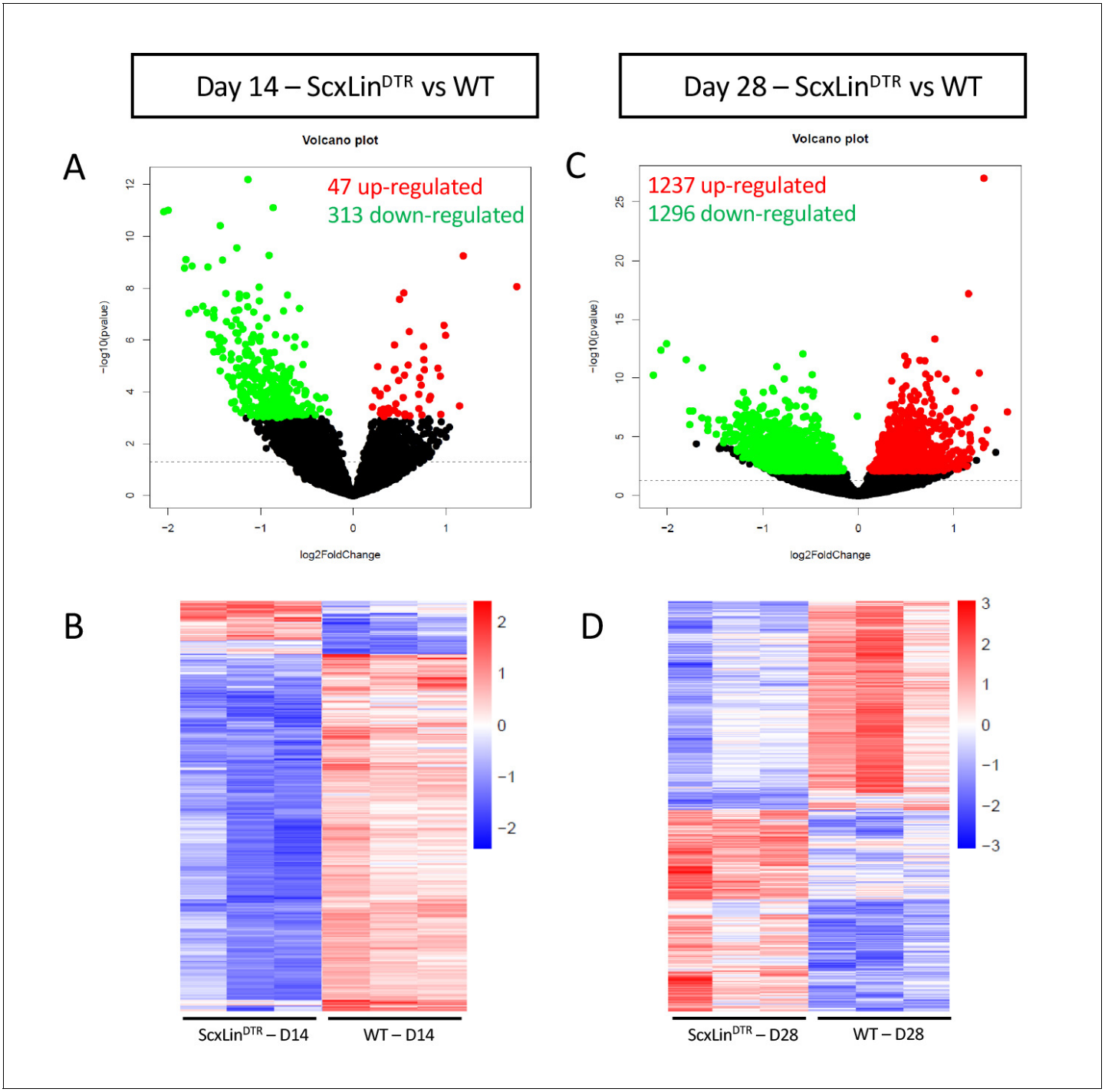

Figure 6. Bulk RNA sequencing reveals differences between ScxLin^{DTR} and wild-type healing flexor tendons at 14 and 28 days post-repair. Representation of differentially expressed genes (DEGs) at 14 (**A, B**) and 28 (**C, D**) days post-repair. Volcano plots (**A, C**) depict significantly upregulated DEGs as red dots and significantly downregulated DEGs as green dots. DEGs are consider significant when the multiple test corrected (adjusted) p-value is $\leq$ 0.05. The dotted line represents the unadjusted p-value of 0.05. Heat maps (**B, D**) depict all significant DEGs, with the data representing the regularized log transformation of the normalized count data.

The online version of this article includes the following figure supplement(s) for figure 6:

Figure supplement 1. Enhanced expression specific matrix components is observed in ScxLin^{DTR} tendon repairs at D28.

significant increase in dispersion compared to all regions of WT (***Figure 9—figure supplement 1E***).

Table 1. Ingenuity pathway analysis downstream effects - Disease and Functions.
Table of all disease and function annotations marked as significant ($p \leq 0.05$ and ABS(Z-score)>2) using IPA core analysis for $ScxLin^{DTR}$ vs WT at day 28 post-repair.

Disease or function annotation		p-value	Activation state	Z-Score
Down-Regulated	**Contractility of skeletal muscle**	**4.96E-16**	**Decreased**	**−3.595**
	Abnormal bone density	0.000000572	Decreased	−3.299
	Contractility of muscle	8.91E-16	Decreased	−2.636
	Intestinal cancer	6.76E-46	Decreased	−2.561
	Bleeding	0.00000075	Decreased	−2.424
	Malignant neoplasm of large intestine	8.42E-46	Decreased	−2.343
	Colorectal cancer	6.67E-23	Decreased	−2.343
	Large intestine neoplasm	2.97E-46	Decreased	−2.256
	Colorectal tumor	1.28E-23	Decreased	−2.256
	Function of muscle	6.93E-14	Decreased	−2.245
	Consumption of oxygen	0.000000942	Decreased	−2.237
	Function of skeletal muscle	1.59E-08	Decreased	−2.186
	Intestinal tumor	9.72E-47	Decreased	−2.144
	Development of lung carcinoma	0.000000663	Decreased	−2.012
Up-regulated	Cell movement	4.98E-22	Increased	4.735
	Migration of cells	6.44E-17	Increased	4.733
	Cell movement of tumor cell lines	8.66E-10	Increased	4.343
	Reorganization of cytoskeleton	0.000000218	Increased	4.296
	Migration of tumor cell lines	0.00000032	Increased	4.162
	Engulfment of cells	1.05E-09	Increased	4.057
	Endocytosis	1.2E-11	Increased	3.821
	Leukocyte migration	4.37E-09	Increased	3.821
	Cell movement of blood cells	4.04E-09	Increased	3.818
	Homing of cells	0.00000055	Increased	3.792
	Formation of cellular protrusions	1.53E-14	Increased	3.669
	Glucose metabolism disorder	5.46E-10	Increased	3.516
	Invasion of cells	9.21E-08	Increased	3.396
	Organization of cytoplasm	3.25E-26	Increased	3.384
	Organization of cytoskeleton	2.94E-20	Increased	3.384
	Cell movement of leukocytes	7.74E-08	Increased	3.38
	Endocytosis by eukaryotic cells	1.16E-08	Increased	3.371
	Engulfment of tumor cell lines	0.00000031	Increased	3.348
	Proliferation of neuronal cells	3.67E-09	Increased	3.313
	Metabolism of carbohydrate	1.94E-13	Increased	3.285
	Formation of lamellipodia	0.000000932	Increased	3.121
	Cell movement of breast cancer cell lines	0.000000603	Increased	3.103
	Cell movement of fibroblast cell lines	3.42E-08	Increased	3.083
	Growth of neurites	6.25E-09	Increased	2.981
	Microtubule dynamics	5.21E-18	Increased	2.974
	Cell spreading	3.31E-11	Increased	2.875
	Formation of filopodia	0.000000177	Increased	2.873
	Cell movement of connective tissue cells	0.000000415	Increased	2.792

Table 1 continued on next page

Table 1 continued

Disease or function annotation		p-value	Activation state	Z-Score
Down-Regulated	**Contractility of skeletal muscle**	**4.96E-16**	**Decreased**	**−3.595**
	Concentration of lipid	3.14E-08	Increased	2.779
	Progressive neurological disorder	6.74E-10	Increased	2.671
	Outgrowth of neurites	7.31E-08	Increased	2.662
	Production of reactive oxygen species	6.22E-12	Increased	2.625
	Quantity of macropinosomes	0.000000865	Increased	2.621
	Neuromuscular disease	1.47E-15	Increased	2.619
	Progressive myopathy	1.28E-11	Increased	2.611
	Synthesis of carbohydrate	0.000000499	Increased	2.553
	Outgrowth of cells	0.000000025	Increased	2.52
	Advanced malignant tumor	0.000000208	Increased	2.517
	Differentiation of connective tissue cells	1.48E-09	Increased	2.512
	Secondary tumor	0.000000643	Increased	2.461
	Arrhythmia	2.14E-08	Increased	2.4
	Fibrosis	0.000000337	Increased	2.397
	Extension of cellular protrusions	0.00000098	Increased	2.371
	Invasive tumor	2.47E-08	Increased	2.345
	Synthesis of reactive oxygen species	3.6E-14	Increased	2.312
	Organization of actin cytoskeleton	4.37E-08	Increased	2.298
	Disassembly of filaments	0.000000544	Increased	2.27
	Metabolism of reactive oxygen species	2.61E-15	Increased	2.269
	Cancer of cells	9.31E-14	Increased	2.254
	Response of tumor cell lines	2.31E-08	Increased	2.231
	Morphogenesis of neurons	1.44E-12	Increased	2.224
	Neuritogenesis	1.86E-12	Increased	2.224
	Neoplasia of cells	1.76E-16	Increased	2.221
	Quantity of metal	0.0000002	Increased	2.198
	Ruffling	0.000000297	Increased	2.157
	Tubulation of cells	0.00000126	Increased	2.132
	Angiogenesis	4.02E-15	Increased	2.109
	Hereditary myopathy	1.58E-23	Increased	2.104
	Dystrophy of muscle	1.85E-11	Increased	2.104
	Development of vasculature	2.67E-16	Increased	2.06
	Growth of axons	0.000000724	Increased	2.017
	Migration of fibroblast cell lines	0.000000461	Increased	2.002

These data suggest a potential relationship between the increased cellularity and fibril dispersion levels on the top region of the ScxLin^{DTR} FTs.

Given these changes in collagen alignment, we further assessed the ECM structure using TEM. (***Figure 9—figure supplement 2A and B***). Collagen fibril diameter distribution was substantially altered between WT (median = 147.95, Q1 = 118.73, Q3 = 179.45) and ScxLin^{DTR,10weeks} (median = 213.41, Q1 = 167.49, Q3 = 261.91) (***Figure 9—figure supplement 2C***). Collagen fibril diameter of ScxLin^{DTR,10weeks} increased by 30.67% compared to WT ($p<0.0001$) (***Figure 9—figure supplement 2D***). The collagen fibril density of ScxLin^{DTR,10weeks} decreased by 48.72% compared to

Table 2. Regulation of matrix components in ScxLin^{DTR} healing tendons at day 28.
Expression level, fold change, and adjusted p-value of key matrix-related genes in ScxLin^{DTR} tendons vs WT at day 28 post-repair generated from bulk RNA-seq. Orange color indicative of increased expression and blue color indicative of decreased expression.

Gene	BaseMean	Fold change (Log_2)	p-adj
Collagens			
Col1a1	742982.883	0.275	0.117206
Col1a2	720257.233	0.359	0.033355
Col2a1	461.965	0.176	0.700754
Col3a1	748380.28	0.645	0.005567
Col4a1	35181.773	0.17	0.559295
Col4a2	31627.065	0.265	0.206116
Col4a3	49.144	−0.009	0.988635
Col4a4	143.52	0.232	0.589161
Col4a5	284.059	0.372	0.440755
Col4a6	52.693	−0.093	0.904823
Col5a1	118821.857	0.495	0.031814
Col5a2	105087.042	0.46	0.092164
Col5a3	35303.666	0.418	0.06355
Col6a1	122410.423	0.406	0.00366
Col6a2	122396.322	0.455	0.003183
Col6a3	55660.629	0.545	0.021485
Col6a4	33.599	−0.879	0.0385
Col6a5	72.046	0.599	0.286724
Col6a6	51.234	−0.07	0.901424
Col7a1	2215.503	−0.532	0.06829
Col8a1	6553.562	0.983	0.025451
Col8a2	4787.689	−0.128	0.727708
Col9a1	390.971	−1.328	0.000857
Col9a2	50.18	−0.071	0.911757
Col9a3	52.911	0.177	0.713852
Col10a1	4.585	0.254	N/A*
Col11a1	13080.117	−0.239	0.496276
Col11a2	1974.589	−0.671	0.028981
Col12a1	34791.768	−0.204	0.545342
Col13a1	308.833	−0.085	0.853468
Col14a1	7279.653	0.693	0.00124
Col15a1	8889.517	0.385	0.296359
Col16a1	24279.347	0.237	0.252556
Col17a1	269.42	0.002	N/A*
Col18a1	14754.886	0.391	0.169961
Col19a1	4.738	0.133	N/A*
Col20a1	438.526	−0.7	0.060808
Col22a1	2064	−0.797	0.022217
Col23a1	4457.185	−0.636	0.025351
Col24a1	966.961	−0.35	0.047102
Col25a1	118.033	0.022	0.975523

Table 2 continued on next page

Table 2 continued

Gene	BaseMean	Fold change (Log_2)	p-adj
Col26a1	78.9	0.371	0.475453
Col27a1	4062.784	0.406	0.253217
Col28a1	579.441	0.291	0.653743
ECM proteoglycans			
Hspg2	47213.867	0.248	0.108795
Aspn	19143.191	0.839	0.007556
Bgn	151131.153	0.251	0.256881
Dcn	95817.718	0.654	1.26E-05
Fmod	132295.748	0.172	0.683103
Kera	5207.231	0.522	0.154489
Lum	43114.099	0.353	0.130133
Omd	65.324	0.56	0.151367
Prelp	18853.124	0.381	0.057946
Epyc	133.935	1.187	0.003793
Ogn	5228.656	0.636	0.004079
Optc	30.193	0.042	0.957221
Chad	2558.426	−0.133	0.813626
Chadl	146.381	0.377	0.295306
Nyx	21.048	0.443	0.360179
Podn	1763.369	0.432	0.131578
Podnl1	216.612	−0.087	0.872241
Acan	8738.435	−0.407	0.194754
Bcan	125.867	−0.764	0.014902
Ncan	1.472	−0.047	N/A*
Vcan	5214.463	0.431	0.165678
Hapln1	109.201	0.036	0.955062
Hapln2	8.84	−0.024	N/A*
Hapln3	31.92	0.039	0.949531
Hapln4	128.699	0.053	0.926101
Prg2	2.717	−0.083	N/A*
Spock1	12.387	0.674	N/A*
Spock2	621.489	0.027	0.956371
Spock3	34.16	−0.034	0.963822
Prg4	26463.024	−0.191	0.759532
Srgn	1500.611	−0.08	0.843956
Impg2	49.211	−0.196	0.676547
Esm1	120.466	−0.02	0.971642
Basement membrane components			
Lama1	3.29	−0.445	N/A*
Lama2	3430.887	0.361	0.201711
Lama3	104.957	−0.303	0.484039
Lama4	7706.819	0.34	0.081572
Lama5	3390.382	−0.237	0.430648
Lamb1	11272.507	0.236	0.389409

Table 2 continued on next page

Table 2 continued

Gene	BaseMean	Fold change (Log_2)	p-adj
Lamb2	13730.5	0.343	0.092701
Lamb3	77.394	−0.06	0.924993
Lamc1	15292.13	0.313	0.119095
Lamc2	424.266	0.393	0.064032
Lamc3	21.597	0.093	0.886633
Nid1	12717.306	0.539	0.02301
Nid2	2799.817	0.179	0.586124
Colq	358.747	−0.379	0.341156
Major ECM glycoproteins			
Eln	17607.464	0.518	0.270402
Emilin1	6960.539	0.124	0.684821
Emilin2	4405.463	0.512	0.061758
Emilin3	595.356	0.857	0.005562
Emid1	550.685	0.252	0.631487
Fbln1	2214.023	0.23	0.320082
Fbln2	48333.486	0.127	0.615495
Fbln5	2725.675	0.326	0.023116
Fbln7	4562.409	0.784	0.00233
Efemp1	1308.939	0.543	0.077648
Efemp2	4858.991	0.222	0.11327
Fbn1	36959.196	0.668	0.005087
Fbn2	2856.248	−0.008	0.983466
Fn1	510510.053	0.307	0.223595
Fras1	430.729	−0.837	0.013797
Gldn	464.82	0.424	0.390168
Hmcn1	1034.806	0.589	0.036404
Hmcn2	6034.922	0.252	0.456036
Ibsp	2.365	−0.125	N/A*
Matn1	0.671	0.074	N/A*
Matn2	6213.381	0.503	0.015668
Matn3	201.369	−0.581	0.155595
Matn4	2796.498	−0.245	0.6134
Mfap1a	536.887	0.101	0.639732
Mfap1b	398.958	0.03	0.902813
Mfap2	3608.727	0.465	0.013072
Mfap3	1213.924	0.119	0.519005
Mfap4	4217.93	0.4	0.210242
Mfap5	14548.008	0.753	5.34E-05
Mmrn1	439.183	0.492	0.262418
Mmrn2	1557.776	−0.201	0.519886
Npnt	1084.388	−0.453	0.209896
Papln	16.561	−0.122	0.859483
Postn	102294.871	0.591	0.048873
Sparc	331616.177	0.479	0.000296

Table 2 continued on next page

Table 2 continued

Gene	BaseMean	Fold change (Log_2)	p-adj
Sparcl1	12872.967	−0.027	0.959288
Spp1	29368.724	0.234	0.637831
Srpx2	5778.794	0.362	0.077229
Tnc	28609.297	0.378	0.326135
Tnn	5098.501	−0.623	0.126873
Tnr	19.271	0.482	0.385953
Tnxa	6.323	0.944	N/A*
Tnxb	18888.425	0.781	0.015263
Thbs1	14477.798	0.49	0.099587
Thbs2	36613.787	0.39	0.149809
Thbs3	17595.855	0.267	0.193149
Thbs4	203095.542	0.841	5.69E-05
Comp	35501.759	0.293	0.10314

WT ($p<0.0001$) (***Figure 9—figure supplement 2E***). Finally, both the WT and the $ScxLin^{DTR,10weeks}$ groups exhibited similar levels of fibril irregularity ($p=0.9023$) (***Figure 9—figure supplement 1F***).

Discussion

Previous work has established the importance of *Scx* expression in tendon development (***Murchison et al., 2007***), growth (***Gumucio et al., 2020***), and healing (***Sakabe et al., 2018***), but few studies have considered the direct contributions of Scx^{Lin} tendon cells to these processes. In the present study, we examined the function of Scx^{Lin} tendon cells during adult flexor tendon healing and made the surprising discovery that Scx^{Lin} cell depletion prior to tendon injury and repair significantly enhanced biomechanical properties by day 28 post-repair. We characterized key cell populations known to be important in healing and regeneration and utilized RNA-Seq to investigate the mechanism driving these biomechanical changes. Lastly, we examined the effects of Scx^{Lin} cell depletion on post-natal tendon growth and adult tendon homeostasis and found that Scx^{Lin} cells are required for maintenance of collagen ECM alignment and organization in adult, but not early post-natal flexor tendon growth.

Tendon cell depletion had surprisingly beneficial effects on healing, with biomechanical properties significantly increased at day 28 post-repair relative to WT, with no impact on gliding function. These results indicate that the improved biomechanical properties are likely not due to increased levels of disorganized matrix/scar within the healing tendon, but that the healing process may be shifted toward a regenerative phenotype. Equally striking is that the significant improvements in biomechanical properties did not emerge until 28 days post-repair, which is firmly into the remodeling phase of healing and is consistent with the low DEG number at day 14 post-repair relative to day 28. This suggests that Scx^{Lin} cells are important in the late proliferative-remodeling phases of healing and possibly enact their greatest effects by modulating the remodeling process. Consistent with this is the lack of difference in proportion of $ScxLin^{Ai9}$ cells at D14 between WT and $ScxLin^{Ai9DTR}$, while a significant decrease in $ScxLin^{Ai9}$ cells was observed in $ScxLin^{Ai9DTR}$ tendon repairs, relative to WT, at D28. While further studies are needed to completely define this process, these data suggest that 'new' Scx^{Lin} cells (e.g. those that express *Scx* in response to tendon injury and are therefore labeled as $ScxLin^{Ai9}$, but that were not Scx^{LinAi9} at the time of depletion) may predominate during early healing, so the effects of depleting Scx^{Lin} prior to injury are minimal. However, by D28 these 'new' $ScxLin^{Ai9}$ cells may undergo apoptosis and be cleared during progressive tissue remodeling, such that the cells that remain at D28 are primarily derived from the $ScxLin^{Ai9}$ cells present in the adult tendon prior to injury. Therefore, the effects of $ScxLin^{Ai9DTR}$ become more apparent and allow interrogation of the functional effects on healing of depleting adult tendon resident Scx^{Lin} cells by D28. Finally, it

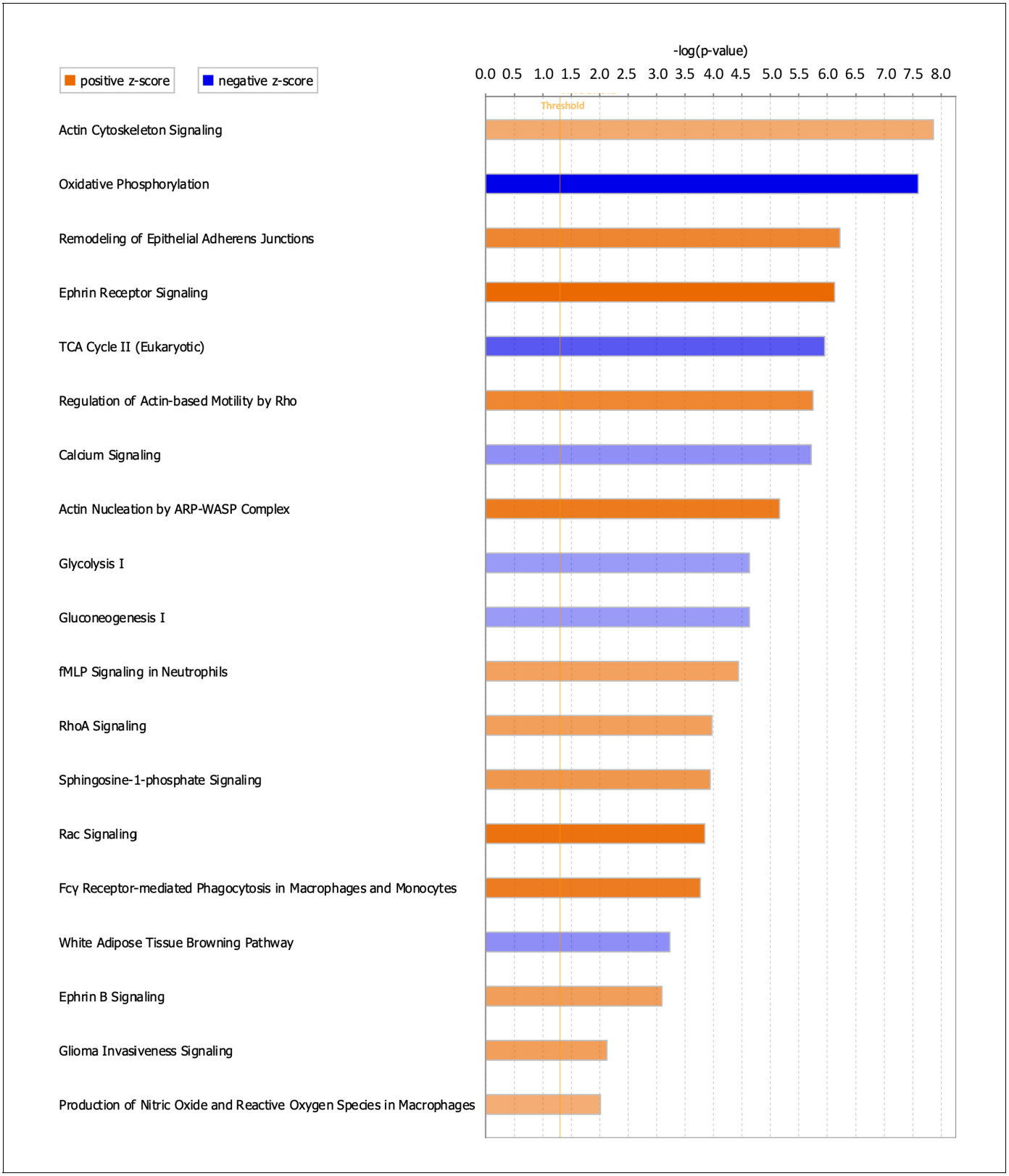

Figure 7. Canonical pathways positively and negatively enriched in ScxLin^{DTR} healing tendons at day 28 post-repair. Ingenuity pathway analysis was utilized to determine positively and negatively significantly enriched pathways in ScxLin^{DTR} healing tendons at day 28 post-repair. Canonical pathways were considered significant if $p<0.05$ and ABS(Z-score)>2. The orange color indicates pathways that are significantly, positively enriched ('activated'),

Figure 7 continued on next page

Figure 7 continued

while the blue color indicates significantly, negatively enriched ('inhibited') pathways. The orange dotted line represents -log (1.3)=0.05, indicating the p-value cut-off.

is also possible that there is a compensatory response by other tenocyte subpopulations. While we do not see any changes in S100a4^{+} cells, it is possible that there may be an increase in S100a4-lineage cells, which can express *Scx* during tendon healing (***Best and Loiselle, 2019***), or other cells.

Our RNA-Seq results revealed significant changes in matrix-related gene expression at day 28 post-repair, suggesting that the matrix composition of the healing tendon may be substantially altered in the absence of Scx^{Lin} cells, with a shift toward either a more regenerative or mature matrix composition. Future proteomics analysis and additional experimentation will be required to further examine the matrix differences between ScxLin^{DTR} and WT healing flexor tendons. It has previously been reported that tendon strength remains significantly decreased relative to uninjured controls 63 days post-repair using this flexor tendon repair model in C57Bl/6J mice (***Loiselle et al., 2009***). Therefore, it could be beneficial to examine time points beyond day 28 to see if ScxLin^{DTR} tendons reach equivalency with uninjured controls. The improved biomechanical properties contrasted with our original hypothesis which predicted that *Scx*^{Lin} cells would be necessary for proper healing and would contribute to formation of the bridging collagen tissue. Both ScxLin^{DTR} and WT mice exhibited a collagen bridge at 14- and 28 days post-repair suggesting that the Scx^{Lin} cells targeted for depletion prior to injury are not the predominant cell population laying down this collagenous matrix. This is surprising due to studies demonstrating that *Scx* promotes collagen formation (***Sakabe et al., 2018***; ***Leéjard et al., 2007***), highlighting the important distinction between Scx^{Lin} cells and active *Scx* expression.

While myofibroblast persistence is considered a primary driver of fibrosis (***Hinz and Lagares, 2020***), recent work has revealed that myofibroblasts are a highly heterogenous population with

Table 3. Ingenuity pathway analysis canonical pathways.
All enriched pathways marked as significant (-log(p-value)>1.3 and ABS(Z-score)>2) using IPA core analysis for ScxLin^{DTR} vs WT at day 28 post-repair.

Canonical pathway		-log(p)	Z-Score
Negatively enriched	**Oxidative phosphorylation**	**7.6**	**−5.303**
	TCA Cycle II (Eukaryotic)	5.96	−3.464
	White Adipose Tissue Browning Pathway	3.23	−2.353
	Calcium Signaling	5.72	−2.335
	Glycolysis I	4.63	−2.111
	Gluconeogenesis I	4.63	−2.111
Positively enriched	Ephrin Receptor Signaling	6.13	3.888
	Rac Signaling	3.85	3.674
	Actin Nucleation by ARP-WASP Complex	5.16	3.441
	Fcγ Receptor-mediated Phagocytosis in Macrophages and Monocytes	3.77	3.411
	Remodeling of Epithelial Adherens Junctions	6.23	3.162
	Regulation of Actin-based Motility by Rho	5.75	3.128
	Sphingosine-1-phosphate Signaling	3.94	2.711
	Ephrin B Signaling	3.09	2.53
	RhoA Signaling	3.97	2.502
	Glioma Invasiveness Signaling	2.13	2.496
	fMLP Signaling in Neutrophils	4.44	2.449
	Actin Cytoskeleton Signaling	7.86	2.214
	Production of Nitric Oxide and Reactive Oxygen Species in Macrophages	2.01	2.117

Table 4. Ingenuity pathway analysis upstream regulators.
All possible upstream regulators where expression log ratio ≥ 0.5, ABS(Z-score)>2, p-value<0.05, and agreement between predicted activation state and directionality of regulator's gene expression, compiled using IPA core analysis for ScxLin^{DTR} vs WT at day 28 post-repair.

Upstream regulator	Expression log ratio	Predicted activation state	Activation Z-score	p-value of overlap
Activated in ScxLin^{DTR}				
S100A4	0.518	Activated	2.946	0.00456
F2	0.533	Activated	2.606	0.000134
BTNL2	0.805	Activated	2.324	0.012
EBF2	0.657	Activated	2.223	0.000738
F2R	0.599	Activated	2.22	0.0243
NTRK2	0.608	Activated	2.137	0.012
SOX2	1.138	Activated	2.071	0.0000143
FGF2	0.544	Activated	2.017	0.000393
Inhibited in ScxLin^{DTR}				
FOXO4	−0.501	Inhibited	−2.697	0.0236
MEF2C	−0.905	Inhibited	−2.577	3.06E-08
SMYD1	−0.836	Inhibited	−2.219	2.63E-12
LDHB	−0.609	Inhibited	−2.219	0.000241

differences in pro-fibrotic markers, gene expression, and cross-linking ability, suggesting that myofibroblasts contribute to both fibrotic and regenerative processes (***Shook et al., 2018***). Despite the elevated myofibroblast presence in ScxLin^{DTR} repairs at day 28, these tendons healed with increased biomechanical properties while experiencing no deficits in tendon range of motion, suggesting a regenerative rather than fibrotic healing process. Future work to comprehensively define the myofibroblast landscape in both WT and ScxLin^{DTR} mice is necessary to determine if ScxLin^{DTR} myofibroblasts are more 'pro-regenerative' than those present in WT repairs. Similarly, understanding how myofibroblast subtypes affect matrix deposition at the repair site represents an important area of future study. Related to this, previous work has shown that regeneration is mediated in large part by the immune response, including macrophages (***Vagnozzi et al., 2020***). However, we did not see any differences in overall macrophage content, or in pathways related to immune response in the RNA-seq. Future work, including single-cell RNA sequencing studies will be important to provide a comprehensive understanding of how Scx^{Lin} cell depletion alters the overall cellular environment and how this dictates the functional changes that are observed.

The RNA-seq data suggests that healing ScxLin^{DTR} tendons exhibit less overall metabolic activity compared to WT repairs at day 28. This is highlighted in IPA's canonical pathways core analysis, where 'Oxidative Phosphorylation,' 'TCA Cycle II,' 'Glycolysis I,' and 'Gluconeogenesis I' were all predicted to be negatively enriched ('suppressed') (***Figure 7***, ***Table 3***). Additionally, IPA's disease and function core analysis predicts an inhibitory effect on 'Consumption of oxygen,' while simultaneously predicting 'Metabolism of carbohydrate' activation, increased 'Synthesis of carbohydrate,' and 'Glucose metabolism disorder (***Table 1***)." It has previously been demonstrated in a variety of tissues that metabolic reprogramming is important for cellular differentiation and regeneration (***Chen et al., 2019***; ***De Santa et al., 2019***; ***Osuma et al., 2018***; ***Lai et al., 2019***). In addition to the dysregulation of metabolism, our RNA-seq data also revealed an increase in 'Production of reactive oxygen species', 'Synthesis of reactive oxygen species', and 'Metabolism of reactive oxygen species (***Table 1***)'. Despite reactive oxygen species (ROS) being implicated in various pathologies (***Schieber and Chandel, 2014***), recent studies have also identified functional roles for ROS in regeneration (***Santabárbara-Ruiz et al., 2019***; ***Youm et al., 2019***; ***Labit et al., 2018***; ***Santabárbara-Ruiz et al., 2015***). While little is currently understood about the role of metabolism and ROS in tendon healing, these data clearly identify how changes in the cellular composition of the healing tendon can shift both the metabolic profile and the healing program. As such, investigating metabolic

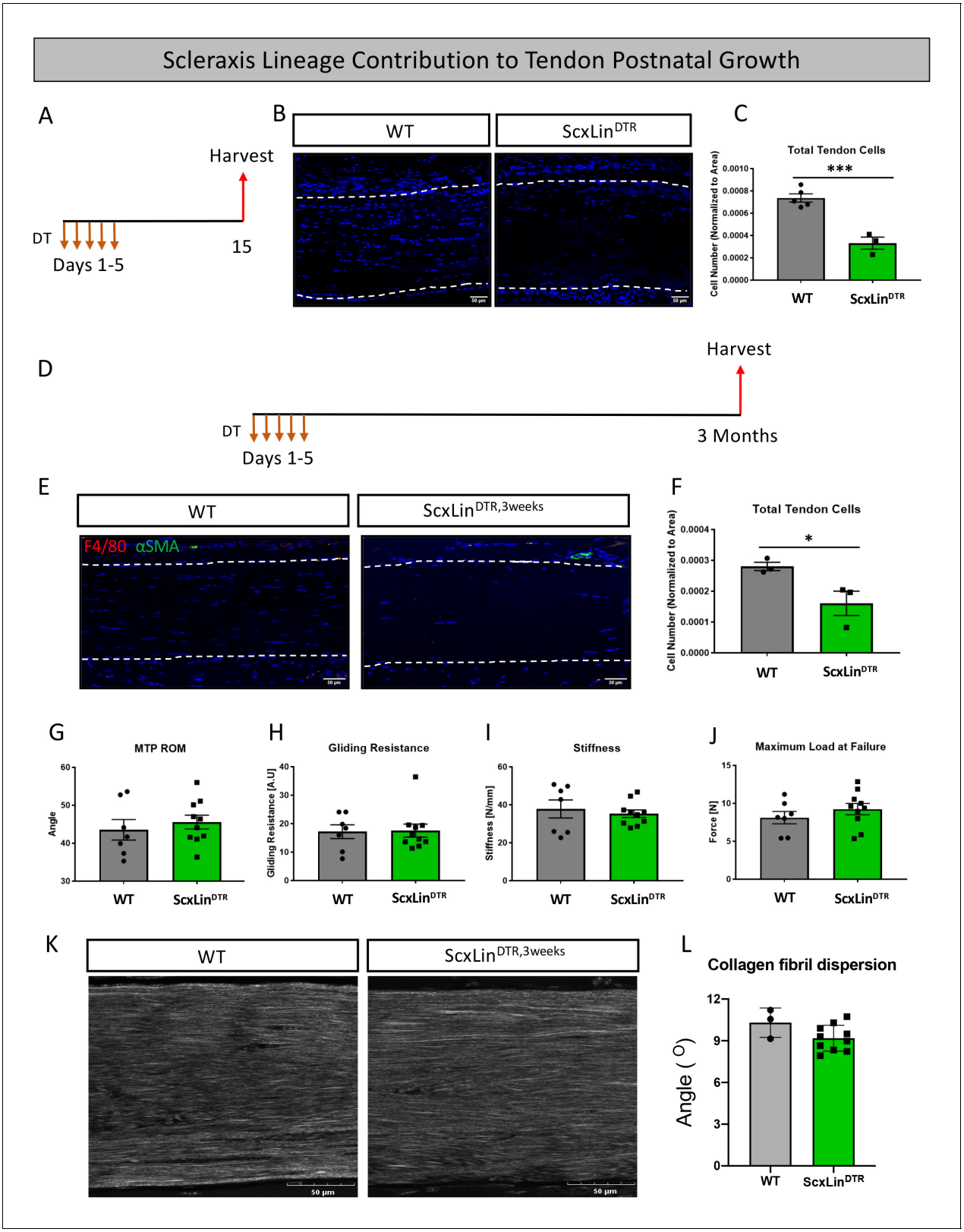

Figure 8. Tendon cell ablation does not negatively affect post-natal tendon growth 3 months post-ablation. Pre-pubescent mice (3–4 weeks old) received five hindpaw injections of DT and were harvested 10 days after the final injection to assess tendon cell depletion (ScxLin^{DTR}) (**A**). Hindpaw sections from both WT and ScxLin^{DTR} hindpaws (**B**). Quantification of WT and ScxLin^{DTR,3weeks} tendon cell number in pre-pubescent mice (**C**). To assess effects of tendon cell depletion on post-natal tendon growth, mice received five hindpaw injections of DT on consecutive days at 3–4 weeks of age and

Figure 8 continued on next page

Figure 8 continued

were harvested uninjured 3 months later for biomechanical, gliding, and histological evaluation (ScxLin^{DTR,3weeks}) (**D**). Co-immunofluorescence of F4/80 (macrophages) and αSMA (myofibroblasts) in uninjured WT and ScxLin^{DTR,3weeks} tendons (**E**). Quantification of WT and ScxLin^{DTR,3weeks} tendon cell number (**F**). Measurement of metatarsophalangeal (MTP) joint flexion angle (**G**), gliding resistance (**H**), stiffness (**I**), and maximum load at failure (**J**) of WT and ScxLin^{DTR,3weeks} uninjured tendons. N = 7–10 per genotype. Second harmonic generation (**K**) and quantification (**L**) of collagen fibril dispersion of WT and ScxLin^{DTR,3weeks}. N = 3 per genotype. Nuclei stained with DAPI. Tendon is outlined by white dotted lines. Student's t-test used to assess statistical significance between genotypes. * indicates $p<0.05$, *** indicates $p<0.001$.

reprogramming and the dynamic roles of ROS in acute tendon healing represents an exciting area of future work.

In addition to investigating the role of tendon cells during healing, we also utilized ScxLin^{DTR} mice to assess how tendon cell ablation affected post-natal tendon growth (ScxLin^{DTR,3weeks}) and adult tendon homeostasis (ScxLin^{DTR,10weeks}). Although there were no significant differences in gliding function or biomechanical properties between ScxLin^{DTR} and WT genotypes in either age group, ScxLin^{DTR,10weeks} animals exhibited significantly increased overall collagen fibril dispersion, as well as significant changes in dispersion in specific regions of the tendon. While it is unclear what is driving these spatially-specific changes in fibril organization, it is notable that the most profound changes occur in the top epitenon region rather than endotenon, and that this area is consistent with altered and increased cellularity in ScxLin^{DTR,10weeks} tendons, though the identity and function of these cells are as yet unknown. In addition to matrix alignment, ScxLin$^{DTR,\ 10\ weeks}$ also increased collagen fibril diameter as measured by TEM. Interestingly, one potential interpretation of the TEM data relates to the loss of proteoglycans (PGs) on the surface of the collagen fibrils, which normally prevents lateral fusion of collagen fibrils. Numerous in vitro and in vivo studies have shown the importance of the PGs to maintain the normal collagen fibril structure. Using proteinase treatment to remove surface bound PGs, Graham et al., demonstrated lateral collagen fibril aggregation, resulting in fused fibrils with increased diameter (***Graham et al., 2000***). In addition, Decorin-/- tail tendons also demonstrated lateral fusion and increased fibril diameter, relative to WT (***Danielson et al., 1997***). While there is no direct evidence of PG production by Scx+ cells, Scx-/- hearts have decreased PG content (***Barnette et al., 2013***; ***Barnette et al., 2014***), while Sakabe et al., found that Scx-/- tendons lacked fibromodulin production during tendon healing (***Sakabe et al., 2018***). Moreover, recent work has shown that Scx knockdown in adult equine tendon cells alters the PG environment (***Paterson et al., 2020***). Collectively, these data suggest that the increase in fibril diameter observed in ScxLin^{DTR,10weeks} could be due to diminution of PG production following depletion of Scx^{Lin} cells. However, we have not directly tested this, and future proteomic studies will be required to determine if and which specific PGs may be altered following Scx^{Lin} cell depletion. Collectively, these data indicate that loss of Scx^{Lin} cells may be detrimental to tendon tissue maintenance, but that negative biomechanical effects are not yet manifested 3 months post-depletion. Future studies looking beyond the 3-month time-point will be informative to understand the role of tendon cells on maintenance of tendon tissue. It is also possible that negative effects on tendon biomechanical properties could be the result of Scx^{Lin} cell death in non-tendon tissues, such as muscle in the hindpaw (***Mendias et al., 2012***). Despite nearly identical depletion efficiencies between ScxLin^{DTR,3weeks} and ScxLin^{DTR,10weeks} animals, only ScxLin^{DTR,10weeks} tendons exhibited collagen disorganization and differences in fibril size. This suggests possible differences in tendon cell sub-populations present during growth and homeostasis, as well as the potential contribution of extrinsic progenitor populations to tendon growth (***Dyment et al., 2014***), such that depletion could differentially impact post-natal growth and adult tendon homeostasis. Moreover, it is possible that ScxLin^{DTR,3weeks} did not disrupt tendon growth due to more rapid compensation by non-depleted Scx^{Lin} cells, or the addition of 'new' Scx^{Lin} cells during this period of rapid tissue growth.

We had initially planned to deplete tendon cells using the inducible Scx-Cre^{ERT2} crossed to the diphtheria toxin A mouse (***Voehringer et al., 2008***), but insufficient recombination occurred, and targeted cell death was not achieved. Therefore, to successfully deplete tendon cells, Scx-Cre mice were crossed to a diphtheria toxin receptor mouse model (ScxLin^{DTR}) (***Buch et al., 2005***). The initial attempt to deplete cells using this model employed a series of intraperitoneal injections (200 ng/day) and resulted in all ScxLin^{DTR} mice dying within four days of the initial injection while WT animals were unaffected. ScxLin^{DTR} mice likely died due to apoptosis of non-tendon/ligament associated

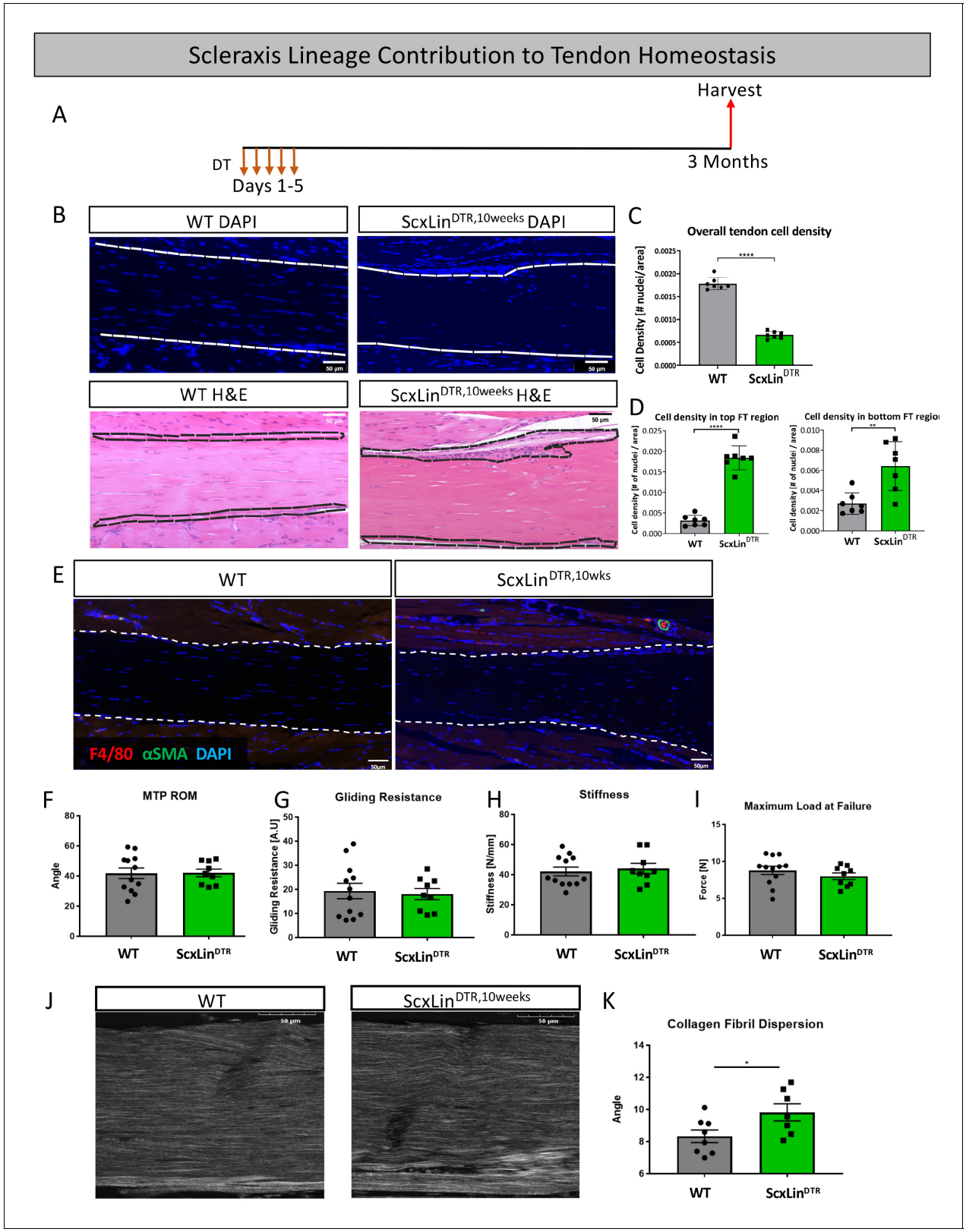

Figure 9. Tendon cell ablation negatively affected tendon homeostasis 3 months post-ablation. Mice received five hindpaw injections of DT on consecutive days at 10–12 weeks of age and were harvested uninjured 3 months later for biomechanical, gliding, and histological evaluation (ScxLin^{DTR,10weeks}) (**A**). Cellularity was assessed using DAPI (**B**) and quantified (**C**) 3 months after Scx^{Lin} cell depletion. H and E staining was used to better define the hypercellular regions near the tendon epitenon. Cell density was quantified at the top and bottom boundaries of the tendon (**D**).

Figure 9 continued on next page

Figure 9 continued

N = 7 per genotype. Co-immunofluorescence of F4/80 (macrophages) and αSMA (myofibroblasts) in uninjured WT and ScxLin^{DTR} tendons (**E**). N = 3 per genotype. Measurement of metatarsophalangeal (MTP) joint flexion angle (**F**), gliding resistance (**G**), stiffness (**H**), and maximum load at failure (**I**) of WT and ScxLin^{DTR,10weeks} uninjured tendons. N = 9–12 per genotype. Second harmonic generation (SHG) (**J**) and quantification (**K**) of collagen fibril dispersion of WT and ScxLin^{DTR,10weeks}. N = 7–8 per genotype. Nuclei stained with DAPI. Tendon is outlined by white dotted lines. Student's t-test used to assess statistical significance between genotypes. * indicates $p<0.05$.
The online version of this article includes the following figure supplement(s) for figure 9:

Figure supplement 1. Collagen fibrils in the top third FT region have an altered organization at 3 months post-depletion.
Figure supplement 2. Collagen fibrils exhibit an altered diameter and density at 3 months post-depletion.

Scx^{Lin} cells. For example, it has previously been shown that *Scx* is expressed in the lung (***Pryce et al., 2007***; ***Perez et al., 2003***), kidney (***Pryce et al., 2007***), muscle (***Mendias et al., 2012***), and brain, (***Perez et al., 2003***) among others. Therefore, to successfully utilize this model of cell depletion while simultaneously preventing ScxLin^{DTR}-associated death, a series of low-dose (20 ng/day) local hind paw injections were administered. We successfully utilized this model of in vivo tendon cell depletion and reached a depletion level of 57%. Therefore, the ScxLin^{DTR} data should be viewed as a model of partial depletion as ~40% of tendon cells remained using this approach. Future work utilizing increased or prolonged DT treatment could be attempted to obtain more complete tendon cell depletion, and to determine if the beneficial effects of tendon cell depletion may be reversed with complete ablation of Scx^{Lin} cells from the tendon. Additionally, our current ScxLin^{DTR} ablation model targets cells prior to injury and thus does not target any cells that turn on *Scx* after injury. It has previously been shown that *Scx* knockout during Achilles tendon healing drives incomplete remodeling of type III collagen to type I collagen (***Sakabe et al., 2018***). As such, it could be interesting to assess if depletion of cells actively expressing *Scx* during healing resulted in deleterious effects on healing. However, local DT injection into the hind paw following repair surgery represents a technical challenge as repeated injections to the healing tendon is likely to disrupt the normal healing process. Moreover, the overlap between those Scx^{Lin} cells in the adult tendon prior to injury, and those that express *Scx* after injury is not yet defined. Finally, while there are likely to be some differences between tendons in terms of the functional contribution of Scx^{Lin} cells to healing process, the type of injury model used is also likely to impact data interpretation. For example, adult Scx^{Lin} cells do not contribute to tissue bridging in a model of Achilles tendon transection without repair (***Howell et al., 2017***), but are found in the bridging tissue following flexor tendon injury and repair (***Best and Loiselle, 2019***). As such, future studies will be needed to clarify if, or how, the functional contribution of Scx^{Lin} cells differ between tendons and injury models.

Altogether, these data demonstrate that Scx^{Lin} cell depletion is beneficial for tendon healing as it increases biomechanical properties several weeks after repair, possibly due to alterations in matrix composition, deposition, and/ or remodeling by αSMA+ myofibroblasts. Moreover, we have identified several molecular pathways that are altered following Scx^{Lin} cell depletion, such as changes in metabolism, cell motility, and the cytoskeleton, which may represent important targets for successfully modulating the healing process. Finally, Scx^{Lin} depletion does not significantly disrupt the biomechanical properties of tendons during early post-natal growth or adult tendon homeostasis within three months of Scx^{Lin} cell depletion. However, given the changes in matrix alignment and organization in adult ScxLin^{DTR} tendons, it is possible that mechanical changes may occur following longer periods of depletion. Understanding the complex nature of tendon cells during healing, growth, and homeostasis can provide us with insights for driving regenerative healing and healthy tendon maintenance in the future.

Materials and methods

Key resources table

Reagent type (species) or resource	Designation	Source or reference	Identifiers	Additional information

Continued on next page

Continued

Reagent type (species) or resource	Designation	Source or reference	Identifiers	Additional information
Genetic reagent (*Mus musculus*)	*Scx*-Cre	Dr. Ronen Schweitzer	MGI:5317938	Referred to as Scx^{Lin} in manuscript
Genetic reagent (*Mus musculus*)	C57BL/6-*Gt(ROSA)26 Sor*$^{tm1(HBEGF)Awai}$/J (*Rosa-DTR*^{LSL})	Jackson Laboratory	Stock #: 007900 RRID:IMSR_JAX:007900	Referred to as $ScxLin^{DTR}$ in manuscript
Genetic reagent (*Mus musculus*)	B6.Cg-Gt(ROSA)26Sortm9 (CAG-tdTomato)Hze/J (*ROSA-Ai9*)	Jackson Laboratory	Stock #: 007909 RRID:IMSR_JAX:007909	Referred to as $ScxLin^{Ai9}$ or $ScxLin^{Ai9DTR}$ in manuscript
Antibody	Anti-SCXA (rabbit polyclonal)	Abcam	Catalog #: ab58655 RRID:AB_882467	(1:500)
Antibody	Anti-S100a4 (rabbit monoclonal)	Abcam	Catalog #: ab197896 RRID:AB_2728774	(1:2000)
Antibody	Anti-cleaved caspase 3 (rabbit polyclonal)	Cell Signalling Technology	Catalog #: 9661 RRID:AB_2341188	(1:100)
Antibody	Anti-PCNA (mouse monoclonal)	Abcam	Catalog #: ab29 RRID:AB_303394	(1:100)
Antibody	Anti-F4/80 (rabbit polyclonal)	Santa Cruz Biotechnology	Catalog #: sc-26643 RRID:AB_2098331	(1:500)
Antibody	Anti-THBS4 (rabbit monoclonal)	Abcam	Catalog #: ab263898	(1:250)
Antibody	Anti-MFAP5 (rabbit monoclonal)	Abcam	Catalog #: ab203828	(1:2000)
Antibody	Anti-Decorin (Rabbit polyclonal)	Abcam	Catalog #: ab175404	(1:250)
Antibody	Anti-alpha-SMA-Cy3 (mouse monoclonal)	Sigma-Aldrich	Catalog #: C6198 RRID:AB_476856	(1:200)
Antibody	Anti-alpha-SMA-FITC (mouse monoclonal)	Sigma-Aldrich	Catalog #: F3777 RRID:AB_476977	(1:500)
Antibody	Rhodamine Red-X (RRX) AffiniPure $F(ab')_2$ Fragment Donkey Anti-Rabbit IgG (H+L) (Donkey polyclonal)	Jackson ImmunoResearch	Catalog #: 711-296-152	(1:200)
Antibody	Alexa Fluor 488 AffiniPure $F(ab')_2$ Fragment Donkey Anti-Goat IgG (H+L) (Donkey polyclonal)	Jackson ImmunoResearch	Catalog #: 705-546-147 RRID:AB_2340430	(1:200)
Antibody	Rhodamine Red-X (RRX) AffiniPure $F(ab')_2$ Fragment Donkey Anti-Mouse IgG (H+L) (Donkey polyclonal)	Jackson ImmunoResearch	Catalog #: 715-296-150 RRID:AB_2340834	(1:200)
Chemical Compound, Drug	Diphtheria Toxin (DT)	Millipore Sigma	D0564-1MG	20 ng DT / injection
Software, algorithms	GraphPad Prism software	GraphPad Prism (https://graphpad.com)	Version 7.02	
Software, algorithms	OlyVIA software	Olympus (https://www.olympus-lifescience.com/en/support/downloads/)	Version 2.9	
Software, algorithms	ImageJ software	ImageJ (http://imagej.nih.gov/ij/)		

Mice

Scx-Cre mice were generously provided by Dr. Ronen Schweitzer. ROSA-$Ai9^{F/F}$ (#007909), and Rosa-DTR^{LSL} (#007900) mice were obtained from the Jackson Laboratory (Bar Harbor, ME, USA). ROSA-$Ai9^{LSL}$ mice express Tomato red fluorescence in the presence of Cre-mediated recombination (***Madisen et al., 2010***). Scx-Cre mice were crossed to ROSA-$Ai9^{F/F}$ mice to label *Scx* lineage cells (Scx^{Lin}). Diphtheria toxin receptor (DTR^{LSL}) mice can be utilized to temporally ablate cell populations

driven by a non-inducible Cre driver (**Buch et al., 2005**). In short, expression of the diphtheria toxin receptor is inhibited prior to Cre-mediated recombination due to the presence of a STOP cassette flanked by loxp site (Loxp-STOP-Loxp; LSL). Following Cre-mediated recombination the STOP cassette is deleted, resulting in expression of DT receptor, in this case specifically on Scx^{Lin} cells. As such, administration of diphtheria toxin (DT) to these mice results in targeted cell death of Scx^{Lin} cells. Scx-Cre mice were crossed to DTR^{LSL} animals to generate a model of Scx^{Lin} tendon cell depletion ($ScxLin^{DTR}$) and Scx-Cre-; DTR^{LSL} littermates were used as wild-type (WT) controls. To simultaneously deplete and visualize Scx^{Lin} tendon cells, Scx-Cre; $Ai9^{F/F}$ mice were crossed to the DTR^{LSL} to generate a model of Scx-Cre^{+}; $Ai9^{F/+}$; $DTR^{F/+}$ littermates ($ScxLin^{Ai9DTR}$) and Scx-Cre^{+}; $Ai9^{F/+}$; $DTR^{+/+}$ ($ScxLin^{Ai9}$)were used as WT to visualize $ScxLin^{Ai9}$ cells without depletion. All mouse studies were performed with 10–12 week-old male and female mice except where otherwise noted (**Figure 7** 3–4-week-old male and female mice). All mouse work (injections, surgeries, harvests) were performed in the morning. Mice were kept in a 12 hr light/dark cycle.

Flexor tendon repair

Complete transection and repair of the murine flexor digitorum longus (FDL) tendon was performed as previously described (**Ackerman and Loiselle, 2016**). Mice received a 15–20 µg injection of sustained-release buprenorphine. Mice were anesthetized with Ketamine (60 mg/kg) and Xylazine (4 mg/kg). To reduce chances of rupture at the repair site, the FDL tendon was first transected at the myotendinous junction and the skin was closed with a 5–0 suture. This MTJ transection results in a transient decrease in tendon loading, with progressive reintegration of the MTJ observed by D7-10 post-surgery. As shown by the absence of αSMA staining in the uninjured tendon adjacent to the repair (**Figure 5—figure supplement 1**), this transient alteration in loading does not induce a widespread tendon response such as degeneration, remodeling, or cellular activation. Next, a small incision was made to the posterior surface of the right hind paw, the FDL tendon was isolated from surrounding tissue and completely transected. The tendon was repaired using 8–0 suture and the skin was closed with a 5–0 suture. Animals resumed prior cage activity, food intake, and water consumption immediately following surgery.

Quantification of tendon cell depletion and Scx^{Lin}cells

$ScxLin^{DTR}$ mice were injected with 20 ng of diphtheria toxin (DT) for five consecutive days (100 ng total DT). Uninjured hind paws were harvested 10 days after the final injection for frozen sectioning. Scx^{Lin} hind paws were harvested uninjured hind paws were fixed in 10% NBF for 24 hr, decalcified in 14% EDTA for four days, and processed in 30% sucrose to cryo-protect the tissue. Samples were embedded using Cryomatrix (Thermo Fisher Scientific, Waltham, MA, USA) and sectioned into 8 mm sagittal sections using an established cryotape-transfer method (**Dyment et al., 2016**). Sections were stained with DAPI to visualize nuclei and imaged using a VS120 Virtual Slide Microscope (Olympus, Waltham, MA). Using Image J, a region of interest (ROI) was drawn around the tendon and an area was obtained. For $ScxLin^{DTR}$ and WT littermate mice, nuclei within the ROI were manually counted and total nuclei number was normalized to area. For Scx^{Lin} mice, fluorescent cells in uninjured sections were manually counted and Scx^{Lin+} cells reported as a percentage of total cells counted in each section. An n = 3–4 (adult mice) or n = 3–5 (young mice) was used for quantification.

Paraffin histology and immunofluorescence

$ScxLin^{DTR}$ hind paws were harvested 10 days after the final DT injection for homeostasis studies, and at 14- and 28 days post-repair. Additionally, uninjured $ScxLin^{DTR}$ hind paws from adult (10–12 weeks) and pre-pubescent (3–4 weeks) mice were harvested 3 months following the final DT injection to assess effects of tendon cell depletion on tendon growth and homeostasis. Hind paws were fixed in 10% neutral buffered formalin (NBF) at room temperature for 72 hr and were subsequently decalcified in Webb Jee EDTA (pH 7.2–7.4) for 7 days at room temperature, processed, and embedded in paraffin. Three-micron sagittal sections were utilized for analysis, except for the 3 month study which were cut at 5-µm to facilitate SHG imaging. $ScxLin^{DTR}$ repair sections were stained with Alcian blue/hematoxylin and Orange G (ABHOG) or Hematoxylin and eosin (H and E) to assess tissue morphology and cellularity, and Masson's Trichrome to assess collagen deposition. For immunofluorescent

staining, sections were stained with Cleaved Caspase 3 (1:100, Cat#: 9661, Cell Signaling, Danvers, MA), PCNA (1:100, Cat#:ab29, Abcam, Cambridge, MA), F4/80 (1:500, Cat#: sc-26643, Santa Cruz, Dallas, TX), α-SMA-CY3 (1:200, Cat#: C6198, Sigma Life Sciences, St. Louis, MO), α-SMA-FITC (1:500, Cat#: F3777, Sigma Life Sciences, St. Louis, MO), S100a4 (1:2000, Cat#: ab197896, Abcam, Cambridge, MA), SCXA (1:500, ab58655, Abcam, Cambridge, MA), Decorin (1:250, Cat # ab175404, Abcam), Thbs4 (1:250, Cat # ab263898, Abcam), Mfap5 (1: 2000, Cat # ab203828, Abcam), or tdTomato (1:500, Cat#: AB8181, SICGEN, Cantanhede, Portugal). Sections were counterstained with the nuclear DAPI stain and imaged with a VS120 Virtual Slide Microscope (Olympus, Waltham, MA).

Quantification of fluorescence

Fluorescent images scanned by the virtual slide scanner were quantified using Visiopharm image analysis software v.6.7.0.2590 (Visiopharm, Hørsholm, Denmark). Automatic segmentation via a threshold classifier was utilized to define and quantify specific cell populations based on fluorescence. An ROI was drawn to encapsulate both the scar tissue and tendon stubs. The area of fluorescent signal was determined and normalized to the total ROI area to determine percentages of each cell type. An n = 4 was used for quantification. Three samples were utilized for quantification of *Scx*+ and *S100a4*+ cells in uninjured ScxLin^{DTR} hind paws 10 days after the final DT injection. Fluorescent cells were manually counted within an ROI and normalized to either the ROI area or to both the ROI area and total cell number.

Quantitative assessment of gliding function and biomechanical properties

Gliding function of uninjured and repaired ScxLin^{DTR} tendons was assessed as previously described (***Hasslund et al., 2008***). Hindlimbs were harvested at the knee-joint and the FDL tendon was disconnected at the myotendinous junction. The FDL tendon was secured between two pieces of tape using superglue and the tendon was loaded incrementally with small weights ranging from 0 to 19 g. Images were captured unloaded and after each load and measurements of the flexion angle of the metatarsophalangeal (MTP) joint were made using Image J. Gliding resistance was derived from the changes in MTP flexion angle over the range of applied loads. An increase in Gliding Resistance and decrease in MTP Flexion Angle is associated with restricted range of motion and increased scar tissue. After conclusion of gliding testing, the FDL tendon was released from the tarsal tunnel while the proximal end of the tendon and the toes of the hind paw were secured into an Instron 8841 uniaxial testing system (Instron Corporation, Norwood, MA). The tendon was loaded until failure at a rate of 30 mm/minute. Seven to 12 samples per genotype per time-point were assessed.

RNA extraction, next-generation sequencing, and data analysis for RNA-Seq

Tendons (three samples per genotype per time point) were harvested at 14- and 28 days post-repair and flash frozen in liquid nitrogen. Total RNA was isolated using the Bullet Blender (Next Advance) to homogenize the tissue. The RNA was isolated from the resulting extract using Trizol (Life Technologies, Carlsbad, CA) and the RNeasy Plus Micro Kit (Qiagen, Valencia, CA) per manufacturer's recommendations. The total RNA concentration was determined with the NanoDrop 1000 spectrophotometer (NanoDrop, Wilmington, DE) and RNA quality assessed with the Agilent Bioanalyzer (Agilent, Santa Clara, CA). The RNA integrity number (RIN) for all harvested samples was 8.4 ± 0.85 (mean ± standard deviation). The TruSeq Stranded mRNA Sample Preparation Kit (Illumina, San Diego, CA) was used for next-generation sequencing library construction per manufacturer's protocols. Briefly, mRNA was purified from 200 ng total RNA with oligo-dT magnetic beads and fragmented. First-strand cDNA synthesis was performed with random hexamer priming followed by second-strand cDNA synthesis using dUTP incorporation for strand marking. End repair and 3' adenylation was then performed on the double-stranded cDNA. Illumina adaptors were ligated to both ends of the cDNA and amplified with PCR primers specific to the adaptor sequences to generate cDNA amplicons of approximately 200–500 bp in size. The amplified libraries were hybridized to the Illumina flow cell and single end reads were generated for each sample using Illumina NovaSeq6000. The generated reads were demultiplexed using bcl2fastq version 2.19.0. Data cleaning and quality control was accomplished using FastP version 0.20.0. Read quantification was

accomplished using subread-1.6.4 package (featureCounts). Data normalization and differential expression analysis of ScxLin^{DTR} relative to WT at a given time point was performed using DESeq2-1.22.1 with an adjusted p-value threshold of 0.05 on each set of raw expression measures. The 'lfcShrink' method was applied, which moderates log2 fold-changes for lowly expressed genes. DeSeq2 data was uploaded to Qiagen's ingenuity pathway analysis (IPA, http://www.ingenuity.com) and submitted to core analysis. Canonical pathways, upstream regulators, and downstream disease and functions were deemed biologically and statistically significant when the calculated ABS(z-score) >2 and p-value<0.05. Additionally, imposed upon the upstream regulator data was an expression log ratio cut-off of 0.5, and agreement between predicted activation state and directionality of expression log ratio. The data consists of three biological replicates per genotype per timepoint. The data generated in this study have been uploaded to the Gene Expression Omnibus under accession number GSE156157.

Second harmonic generation two-photon confocal imaging

Five-micron paraffin sections of WT and ScxLin^{DTR} hind paws were utilized for second harmonic generation (SHG) imaging. Sections were scanned with a Spectra-Physics MaiTai HP DeepSee Ti:Sapphire Laser, tuned to 1000 nm, under 25x magnification, with a 2.5X optical zoom, with a step size of 0.25 µm. 3D projections of image stacks were generated using the 3D-Project macro in ImageJ and analyzed for collagen fibril uniformity using the Directionality macro. The Directionality macro utilizes Fourier transform analysis to derive spatial orientation of image stacks. Three to 10 samples per genotype were used to quantify overall collagen fibril dispersion for pre-pubescent studies, while sections were analyzed from 7 to 8 mice per genotype for the adult homeostasis studies. To quantify spatial dispersion in adult samples, each image stack was divided into equal thirds (top, middle, and bottom), and dispersion was calculated within each region using Directionality macro as above. N = 6 per genotype per age group were used to quantify the spatial collagen fibril dispersion.

Transmission electron microscopy imaging and analysis

FDL tendons were isolated (N = 4 for WT; N = 3 for ScxLin^{DTR,10weeks}) and fixed in Glutaraldehyde Sodium Cacodylate fixative. One-micron axial sections were cut and stained with Toluidine blue. One-micron sections were then trimmed to 70 nm and stained with uranyl acetate and lead citrate. Sections were placed on grids for imaging on a Hitachi 7650 Analytical TEM. Three non-overlapping images were taken from mid-substance of each tendon at ×40,000 magnification. For measurement of fibril diameter, a region of interest (ROI) was determined within each image so that a minimum of 80 fibrils could be measured. Diameters were measured along the y-axis. The perimeter and the area of the collagen fibrils were quantified. The radii based on the calculated perimeter and area were quantified. The ratio of these two radii represent a measure of fibril roundness (fibril irregularity factor; FIF). An FIF different than one suggest that the fibril is not a perfect circle.

Statistical analysis and animal stratification

Experimental N determined based on previously published work (***Best and Loiselle, 2019***; ***Best et al., 2019***). Quantitative data was analyzed via GraphPad Prism and is presented as mean ± standard error of the mean (SEM). Either a student's t-test or two-way analysis of variance (ANOVA) with Sidak's multiple comparisons test was used to analyze data when data was normal. A Mann-Whitney test was utilized when data was not distributed normally [*Scx*+ cells normalized to area and total cell number (***Figure 1—figure supplement 1C***), D28 F4/80 and S100a4 immunofluorescence (***Figure 4***)]. GraphPad Prism was used to detect outlier data points (ROUT method, Q-value = 1%) and no outliers were found. Mice were randomly selected for specific experimental outcome metrics prior to surgery and quantitative data (ex. fluorescence quantification, gliding, and biomechanical properties) were analyzed in a blinded manner. For all experiments, an N = 1 represents one mouse. p values $\leq$ 0.05 were considered significant. * indicates p<0.05, ** indicates p<0.01, *** indicates p<0.001, **** indicates p<0.0001.

Study approval

This study was carried out in strict accordance with the recommendations in the Guide for the Care and Use of Laboratory Animals of the National Institutes of Health. All animal procedures described were approved by the University Committee on Animal Research (UCAR) at the University of Rochester Medical Center.

Acknowledgements

We thank the Histology, Biochemistry and Molecular Imaging (HBMI) and the Biomechanics, Biomaterials and Multimodal Tissue Imaging (BBMTI) for technical assistance with the histology and biomechanical testing, respectively. We would also like to thank the URMC Multiphoton and Analytical Imaging Center (MAGIC) for assistance with Second Harmonic Generation Imaging, the UR Genomics Research Core for assistance with RNA sequencing experiment and the Electron Microscopy Core for assistance with the transmission electron microscopy data.

Additional information

Funding

Funder	Grant reference number	Author
National Institute of Arthritis and Musculoskeletal and Skin Diseases	F31 AR074815	Katherine T Best
National Institute of Arthritis and Musculoskeletal and Skin Diseases	K01AR068386	Alayna E Loiselle
National Institute of Arthritis and Musculoskeletal and Skin Diseases	R01AR073169	Alayna E Loiselle
National Institute of Arthritis and Musculoskeletal and Skin Diseases	R01AR070765	Mark R Buckley
National Institute of Arthritis and Musculoskeletal and Skin Diseases	T32 AR076950	Anne EC Nichols

The funders had no role in study design, data collection and interpretation, or the decision to submit the work for publication.

Author contributions

Katherine T Best, Conceptualization, Formal analysis, Funding acquisition, Methodology, Writing - original draft, Writing - review and editing; Antonion Korcari, Conceptualization, Formal analysis, Methodology, Writing - original draft, Writing - review and editing; Keshia E Mora, Anne EC Nichols, Formal analysis, Methodology, Writing - review and editing; Samantha N Muscat, Formal analysis, Writing - review and editing; Emma Knapp, Data curation, Writing - review and editing; Mark R Buckley, Supervision, Methodology, Writing - review and editing; Alayna E Loiselle, Conceptualization, Supervision, Funding acquisition, Writing - original draft, Writing - review and editing

Author ORCIDs

Alayna E Loiselle https://orcid.org/0000-0002-7548-6653

Ethics

Animal experimentation: This study was performed in strict accordance with the recommendations in the Guide for the Care and Use of Laboratory Animals of the National Institutes of Health. All of the animals were handled according to approval by the University Committee on Animal Resources (UCAR) for protocols #2014-004E and 2017-030 at the University of Rochester. All surgery was performed under ketamine anesthesia, and every effort was made to minimize suffering.

Decision letter and Author response
Decision letter https://doi.org/10.7554/eLife.62203.sa1
Author response https://doi.org/10.7554/eLife.62203.sa2

Additional files

Supplementary files

- Transparent reporting form

Data availability

Sequencing data have been deposited in GEO under accession code GSE156157. All other data generated during this study are included in the manuscript and supporting files.

The following dataset was generated:

Author(s)	Year	Dataset title	Dataset URL	Database and Identifier
Best KT, Loiselle AE	2021	RNA-seq analysis of Scx-lineage cell depletion to investigate tendon cell functions during flexor tendon healing	https://www.ncbi.nlm.nih.gov/geo/query/acc.cgi?acc=GSE156157	NCBI Gene Expression Omnibus, GSE156157

The following previously published datasets were used:

Author(s)	Year	Dataset title	Dataset URL	Database and Identifier
Lincoln J, Barnette DN	2014	Expression data from embryonic day 15.5 atrioventricular canal regions were isolated from Scx-/- and Scx+/+ mice	https://www.ncbi.nlm.nih.gov/geo/query/acc.cgi?acc=GSE57423	NCBI Gene Expression Omnibus, GSE57423
Mendias C, Swanson J	2019	Single cell transcriptional atlas of mouse Achilles tendons	https://www.ncbi.nlm.nih.gov/geo/query/acc.cgi?acc=GSE138515	NCBI Gene Expression Omnibus, GSE138515

References

Ackerman JE, Nichols AE, Studentsova V, Best KT, Knapp E, Loiselle AE. 2019. Cell non-autonomous functions of S100a4 drive fibrotic tendon healing. *eLife* **8**:e45342. DOI: https://doi.org/10.7554/eLife.45342, PMID: 31124787

Ackerman JE, Loiselle AE. 2016. Murine flexor tendon injury and repair surgery. *Journal of Visualized Experiments* **19**:54433. DOI: https://doi.org/10.3791/54433

Al-Hattab DS, Safi HA, Nagalingam RS, Bagchi RA, Stecy MT, Czubryt MP. 2018. Scleraxis regulates Twist1 and Snai1 expression in the epithelial-to-mesenchymal transition. *American Journal of Physiology-Heart and Circulatory Physiology* **315**:H658–H668. DOI: https://doi.org/10.1152/ajpheart.00092.2018, PMID: 29906225

Alberton P, Popov C, Prägert M, Kohler J, Shukunami C, Schieker M, Docheva D. 2012. Conversion of human bone marrow-derived mesenchymal stem cells into tendon progenitor cells by ectopic expression of scleraxis. *Stem Cells and Development* **21**:846–858. DOI: https://doi.org/10.1089/scd.2011.0150, PMID: 21988170

Barnette DN, Hulin A, Ahmed AS, Colige AC, Azhar M, Lincoln J. 2013. Tgfβ-Smad and MAPK signaling mediate scleraxis and proteoglycan expression in heart valves. *Journal of Molecular and Cellular Cardiology* **65**:137–146. DOI: https://doi.org/10.1016/j.yjmcc.2013.10.007, PMID: 24157418

Barnette DN, VandeKopple M, Wu Y, Willoughby DA, Lincoln J. 2014. RNA-seq analysis to identify novel roles of scleraxis during embryonic mouse heart valve remodeling. *PLOS ONE* **9**:e101425. DOI: https://doi.org/10.1371/journal.pone.0101425, PMID: 24983472

Bavin EP, Atkinson F, Barsby T, Guest DJ. 2017. Scleraxis is essential for tendon differentiation by equine embryonic stem cells and in equine fetal tenocytes. *Stem Cells and Development* **26**:441–450. DOI: https://doi.org/10.1089/scd.2016.0279, PMID: 27899062

Best KT, Lee FK, Knapp E, Awad HA, Loiselle AE. 2019. Deletion of NFKB1 enhances canonical NF-κB signaling and increases macrophage and myofibroblast content during tendon healing. *Scientific Reports* **9**:10926. DOI: https://doi.org/10.1038/s41598-019-47461-5, PMID: 31358843

Best KT, Loiselle AE. 2019. Scleraxis lineage cells contribute to organized bridging tissue during tendon healing and identify a subpopulation of resident tendon cells. *The FASEB Journal* **33**:8578–8587. DOI: https://doi.org/10.1096/fj.201900130RR, PMID: 30951381

Buch T, Heppner FL, Tertilt C, Heinen TJ, Kremer M, Wunderlich FT, Jung S, Waisman A. 2005. A Cre-inducible diphtheria toxin receptor mediates cell lineage ablation after toxin administration. *Nature Methods* **2**:419–426. DOI: https://doi.org/10.1038/nmeth762, PMID: 15908920

Chen X, Yin Z, Chen JL, Shen WL, Liu HH, Tang QM, Fang Z, Lu LR, Ji J, Ouyang HW. 2012. Force and scleraxis synergistically promote the commitment of human ES cells derived MSCs to tenocytes. *Scientific Reports* **2**:977. DOI: https://doi.org/10.1038/srep00977, PMID: 23243495

Chen F, Zhou J, Li Y, Zhao Y, Yuan J, Cao Y, Wang L, Zhang Z, Zhang B, Wang CC, Cheung TH, Wu Z, Wong CC, Sun H, Wang H. 2019. YY1 regulates skeletal muscle regeneration through controlling metabolic reprogramming of satellite cells. *The EMBO Journal* **38**:e99727. DOI: https://doi.org/10.15252/embj.201899727, PMID: 30979776

Costa-Almeida R, Calejo I, Gomes ME. 2019. Mesenchymal stem cells empowering tendon regenerative therapies. *International Journal of Molecular Sciences* **20**:3002. DOI: https://doi.org/10.3390/ijms20123002

Danielson KG, Baribault H, Holmes DF, Graham H, Kadler KE, Iozzo RV. 1997. Targeted disruption of decorin leads to abnormal collagen fibril morphology and skin fragility. *Journal of Cell Biology* **136**:729–743. DOI: https://doi.org/10.1083/jcb.136.3.729

De Micheli AJ, Swanson JB, Disser NP, Martinez LM, Walker NR, Oliver DJ, Cosgrove BD, Mendias CL. 2020. Single-cell transcriptomic analysis identifies extensive heterogeneity in the cellular composition of mouse achilles tendons. *American Journal of Physiology-Cell Physiology* **319**:C885–C894. DOI: https://doi.org/10.1152/ajpcell.00372.2020, PMID: 32877217

De Santa F, Vitiello L, Torcinaro A, Ferraro E. 2019. The role of metabolic remodeling in macrophage polarization and its effect on skeletal muscle regeneration. *Antioxidants and Redox Signaling* **30**:1553–1598. DOI: https://doi.org/10.1089/ars.2017.7420, PMID: 30070144

Dyment NA, Hagiwara Y, Matthews BG, Li Y, Kalajzic I, Rowe DW. 2014. Lineage tracing of resident tendon progenitor cells during growth and natural healing. *PLOS ONE* **9**:e96113. DOI: https://doi.org/10.1371/journal.pone.0096113, PMID: 24759953

Dyment NA, Jiang X, Chen L, Hong S-H, Adams DJ, Ackert-Bicknell C, Shin D-G, Rowe DW. 2016. High-Throughput, Multi-Image cryohistology of mineralized tissues. *Journal of Visualized Experiments* **14**:54468. DOI: https://doi.org/10.3791/54468

Graham HK, Holmes DF, Watson RB, Kadler KE. 2000. Identification of collagen fibril fusion during vertebrate tendon morphogenesis the process relies on unipolar fibrils and is regulated by collagen-proteoglycan interaction. *Journal of Molecular Biology* **295**:891–902. DOI: https://doi.org/10.1006/jmbi.1999.3384, PMID: 10656798

Gumucio JP, Schonk MM, Kharaz YA, Comerford E, Mendias CL. 2020. Scleraxis is required for the growth of adult tendons in response to mechanical loading. *JCI Insight* **5**:138295. DOI: https://doi.org/10.1172/jci.insight.138295, PMID: 32463804

Hasslund S, Jacobson JA, Dadali T, Basile P, Ulrich-Vinther M, Søballe K, Schwarz EM, O'Keefe RJ, Mitten DJ, Awad HA. 2008. Adhesions in a murine flexor tendon graft model: autograft versus allograft reconstruction. *Journal of Orthopaedic Research* **26**:824–833. DOI: https://doi.org/10.1002/jor.20531, PMID: 18186128

Hinz B, Lagares D. 2020. Evasion of apoptosis by myofibroblasts: a hallmark of fibrotic diseases. *Nature Reviews Rheumatology* **16**:11–31. DOI: https://doi.org/10.1038/s41584-019-0324-5, PMID: 31792399

Howell K, Chien C, Bell R, Laudier D, Tufa SF, Keene DR, Andarawis-Puri N, Huang AH. 2017. Novel model of tendon regeneration reveals distinct cell mechanisms underlying regenerative and fibrotic tendon healing. *Scientific Reports* **7**:45238. DOI: https://doi.org/10.1038/srep45238, PMID: 28332620

Huang AH, Watson SS, Wang L, Baker BM, Akiyama H, Brigande JV, Schweitzer R. 2019. Requirement for scleraxis in the recruitment of mesenchymal progenitors during embryonic tendon elongation. *Development* **146**:dev182782. DOI: https://doi.org/10.1242/dev.182782, PMID: 31540914

Hynes RO, Naba A. 2012. Overview of the matrisome–an inventory of extracellular matrix constituents and functions. *Cold Spring Harbor Perspectives in Biology* **4**:a004903. DOI: https://doi.org/10.1101/cshperspect.a004903, PMID: 21937732

Kendal AR, Layton T, Al-Mossawi H, Appleton L, Dakin S, Brown R, Loizou C, Rogers M, Sharp R, Carr A. 2020. Multi-omic single cell analysis resolves novel stromal cell populations in healthy and diseased human tendon. *Scientific Reports* **10**:13939. DOI: https://doi.org/10.1038/s41598-020-70786-5, PMID: 32883960

Labit E, Rabiller L, Rampon C, Guissard C, André M, Barreau C, Cousin B, Carrière A, Eddine MA, Pipy B, Pénicaud L, Lorsignol A, Vriz S, Dromard C, Casteilla L. 2018. Opioids prevent regeneration in adult mammals through inhibition of ROS production. *Scientific Reports* **8**:12170. DOI: https://doi.org/10.1038/s41598-018-29594-1, PMID: 30111876

Lai L, Reineke E, Hamilton DJ, Cooke JP. 2019. Glycolytic switch is required for transdifferentiation to endothelial lineage. *Circulation* **139**:119–133. DOI: https://doi.org/10.1161/CIRCULATIONAHA.118.035741, PMID: 30586707

Leéjard V, Brideau G, Blais F, Salingcarnboriboon R, Wagner G, Roehrl MHA, Noda M, Duprez D, Houillier P, Rossert J. 2007. Scleraxis and NFATc regulate the expression of the Pro-α1(I) Collagen gene in tendon fibroblasts. *Journal of Biological Chemistry* **282**:17665–17675. DOI: https://doi.org/10.1074/jbc.M610113200

Levay AK, Peacock JD, Lu Y, Koch M, Hinton RB, Kadler KE, Lincoln J. 2008. Scleraxis is required for cell lineage differentiation and extracellular matrix remodeling during murine heart valve formation in vivo. *Circulation Research* **103**:948–956. DOI: https://doi.org/10.1161/CIRCRESAHA.108.177238, PMID: 18802027

Loiselle AE, Bragdon GA, Jacobson JA, Hasslund S, Cortes ZE, Schwarz EM, Mitten DJ, Awad HA, O'Keefe RJ. 2009. Remodeling of murine intrasynovial tendon adhesions following injury: mmp and neotendon gene expression. *Journal of Orthopaedic Research* **27**:833–840. DOI: https://doi.org/10.1002/jor.20769, PMID: 19051246

Madisen L, Zwingman TA, Sunkin SM, Oh SW, Zariwala HA, Gu H, Ng LL, Palmiter RD, Hawrylycz MJ, Jones AR, Lein ES, Zeng H. 2010. A robust and high-throughput cre reporting and characterization system for the whole mouse brain. *Nature Neuroscience* **13**:133–140. DOI: https://doi.org/10.1038/nn.2467, PMID: 20023653

Maeda T, Sakabe T, Sunaga A, Sakai K, Rivera AL, Keene DR, Sasaki T, Stavnezer E, Iannotti J, Schweitzer R, Ilic D, Baskaran H, Sakai T. 2011. Conversion of mechanical force into TGF-β-mediated biochemical signals. *Current Biology* **21**:933–941. DOI: https://doi.org/10.1016/j.cub.2011.04.007, PMID: 21600772

Mendias CL, Gumucio JP, Davis ME, Bromley CW, Davis CS, Brooks SV. 2012. Transforming growth factor-beta induces skeletal muscle atrophy and fibrosis through the induction of atrogin-1 and scleraxis. *Muscle and Nerve* **45**:55–59. DOI: https://doi.org/10.1002/mus.22232, PMID: 22190307

Murchison ND, Price BA, Conner DA, Keene DR, Olson EN, Tabin CJ, Schweitzer R. 2007. Regulation of tendon differentiation by scleraxis distinguishes force-transmitting tendons from muscle-anchoring tendons. *Development* **134**:2697–2708. DOI: https://doi.org/10.1242/dev.001933, PMID: 17567668

Nichols AEC, Werre SR, Dahlgren LA. 2018a. Transient scleraxis overexpression combined with cyclic strain enhances ligament cell differentiation. *Tissue Engineering Part A* **24**:1444–1455. DOI: https://doi.org/10.1089/ten.tea.2017.0481, PMID: 29644940

Nichols AEC, Settlage RE, Werre SR, Dahlgren LA. 2018b. Novel roles for scleraxis in regulating adult tenocyte function. *BMC Cell Biology* **19**:14. DOI: https://doi.org/10.1186/s12860-018-0166-z, PMID: 30086712

Nichols AEC, Best KT, Loiselle AE. 2019. The cellular basis of fibrotic tendon healing: challenges and opportunities. *Translational Research* **209**:156–168. DOI: https://doi.org/10.1016/j.trsl.2019.02.002, PMID: 30776336

Osuma EA, Riggs DW, Gibb AA, Hill BG. 2018. High throughput measurement of metabolism in planarians reveals activation of glycolysis during regeneration. *Regeneration* **5**:78–86. DOI: https://doi.org/10.1002/reg2.95, PMID: 29721328

Paterson YZ, Evans N, Kan S, Cribbs A, Henson FMD, Guest DJ. 2020. The transcription factor scleraxis differentially regulates gene expression in tenocytes isolated at different developmental stages. *Mechanisms of Development* **163**:103635. DOI: https://doi.org/10.1016/j.mod.2020.103635, PMID: 32795590

Perez AV, Perrine M, Brainard N, Vogel KG. 2003. Scleraxis (Scx) directs lacZ expression in tendon of transgenic mice. *Mechanisms of Development* **120**:1153–1163. DOI: https://doi.org/10.1016/j.mod.2003.08.003, PMID: 14568104

Pryce BA, Brent AE, Murchison ND, Tabin CJ, Schweitzer R. 2007. Generation of transgenic tendon reporters, ScxGFP and ScxAP, using regulatory elements of the scleraxis gene. *Developmental Dynamics* **236**:1677–1682. DOI: https://doi.org/10.1002/dvdy.21179, PMID: 17497702

Pryce BA, Watson SS, Murchison ND, Staverosky JA, Dünker N, Schweitzer R. 2009. Recruitment and maintenance of tendon progenitors by TGFbeta signaling are essential for tendon formation. *Development* **136**:1351–1361. DOI: https://doi.org/10.1242/dev.027342, PMID: 19304887

Sakabe T, Sakai K, Maeda T, Sunaga A, Furuta N, Schweitzer R, Sasaki T, Sakai T. 2018. Transcription factor scleraxis vitally contributes to progenitor lineage direction in wound healing of adult tendon in mice. *Journal of Biological Chemistry* **293**:5766–5780. DOI: https://doi.org/10.1074/jbc.RA118.001987

Santabárbara-Ruiz P, López-Santillán M, Martínez-Rodríguez I, Binagui-Casas A, Pérez L, Milán M, Corominas M, Serras F. 2015. ROS-Induced JNK and p38 signaling is required for unpaired cytokine activation during *Drosophila* Regeneration. *PLOS Genetics* **11**:e1005595. DOI: https://doi.org/10.1371/journal.pgen.1005595, PMID: 26496642

Santabárbara-Ruiz P, Esteban-Collado J, Pérez L, Viola G, Abril JF, Milán M, Corominas M, Serras F. 2019. Ask1 and akt act synergistically to promote ROS-dependent regeneration in *Drosophila*. *PLOS Genetics* **15**:e1007926. DOI: https://doi.org/10.1371/journal.pgen.1007926, PMID: 30677014

Schieber M, Chandel NS. 2014. ROS function in redox signaling and oxidative stress. *Current Biology* **24**:R453–R462. DOI: https://doi.org/10.1016/j.cub.2014.03.034, PMID: 24845678

Schweitzer R, Chyung JH, Murtaugh LC, Brent AE, Rosen V, Olson EN, Lassar A, Tabin CJ. 2001. Analysis of the tendon cell fate using scleraxis, a specific marker for tendons and ligaments. *Development* **128**:3855–3866. PMID: 11585810

Shook BA, Wasko RR, Rivera-Gonzalez GC, Salazar-Gatzimas E, López-Giráldez F, Dash BC, Muñoz-Rojas AR, Aultman KD, Zwick RK, Lei V, Arbiser JL, Miller-Jensen K, Clark DA, Hsia HC, Horsley V. 2018. Myofibroblast proliferation and heterogeneity are supported by macrophages during skin repair. *Science* **362**:eaar2971. DOI: https://doi.org/10.1126/science.aar2971, PMID: 30467144

Vagnozzi RJ, Maillet M, Sargent MA, Khalil H, Johansen AKZ, Schwanekamp JA, York AJ, Huang V, Nahrendorf M, Sadayappan S, Molkentin JD. 2020. An acute immune response underlies the benefit of cardiac stem cell therapy. *Nature* **577**:405–409. DOI: https://doi.org/10.1038/s41586-019-1802-2, PMID: 31775156

Voehringer D, Liang HE, Locksley RM. 2008. Homeostasis and effector function of lymphopenia-induced "memory-like" T cells in constitutively T cell-depleted mice. *The Journal of Immunology* **180**:4742–4753. DOI: https://doi.org/10.4049/jimmunol.180.7.4742, PMID: 18354198

Walia B, Huang AH. 2019. Tendon stem progenitor cells: understanding the biology to inform therapeutic strategies for tendon repair. *Journal of Orthopaedic Research* **37**:1270–1280. DOI: https://doi.org/10.1002/jor.24156, PMID: 30270569

Youm TH, Woo SH, Kwon ES, Park SS. 2019. NADPH oxidase 4 contributes to myoblast fusion and skeletal muscle regeneration. *Oxidative Medicine and Cellular Longevity* **2019**:1–12. DOI: https://doi.org/10.1155/2019/3585390, PMID: 31827673